CHALMERS
UNIVERSITY OF TECHNOLOGY

Spectral Fatigue and LCOE Assessment of Floating Offshore Wind Turbines

Master's thesis in Sustainable Energy Systems

Björn Nembach

DEPARTMENT OF MECHANICS AND MARITIME SCIENCES

CHALMERS UNIVERSITY OF TECHNOLOGY
Gothenburg, Sweden 2022
www.chalmers.se

Master's thesis 2022

Spectral Fatigue and LCOE Assessment of Floating Offshore Wind Turbines

Björn Nembach

CHALMERS
UNIVERSITY OF TECHNOLOGY

Department of Mechanics and Maritime Sciences
Division of Maritime Technology
Chalmers University of Technology
Gothenburg, Sweden 2022

Spectral Fatigue and LCOE Assessment of Floating Offshore Wind Turbines
Björn Nembach

Examiner and Supervisor: Wengang Mao, Department of Mechanics and Maritime Sciences at Chalmers University of Technology
Co-Supervisor at Chalmers: Xiao Lang
Co-Supervisors at University of Stuttgart: Wei Yu & Moritz Gräfe

Master's Thesis 2022:46
Department of Mechanics and Maritime Sciences
Division of Maritime Technology
Chalmers University of Technology
SE-412 96 Gothenburg
Telephone +46 31 772 1000

Typeset in LaTeX
Printed by Chalmers Reproservice
Gothenburg, Sweden 2022

Spectral Fatigue and LCOE Assessment of Floating Offshore Wind Turbines
Björn Nembach
Department of Maritime Technology
Chalmers University of Technology

Abstract

Floating offshore wind turbines (FOWT) are an emerging technology that will contribute towards a more sustainable energy system in the near future. Some of the main challenges in an early design stage of floating offshore wind turbines are the estimation of costs, the site selection and analyzing their fatigue damage. These challenges are investigated in this work for the WindStar TLP system.
In the first part a LCOE-model from the literature for other FOWT concepts is adapted for the WindStar TLP system. The model calculates the costs as a function of the water depth and the distance to the closest shore and puts them in relation to the annual energy production. By using MetOcean-data as input, the LCOE for possible site locations on a grid of the North Sea area are estimated. The results show that the calculated LCOE of the WindStar TLP system is comparable to the LCOE of other concepts from literature. Furthermore, the results show that, based on the LCOE, good locations for floating wind farms are north of Scotland and west of Denmark.

In the second part, four approaches to perform a spectral fatigue assessment using FAST simulations are studied. With the so-called White-Noise approach the fatigue damage for every possible sea state can be calculated with just a very limited number of simulations. The short-term fatigue damage for every approach is calculated using several spectral approximation methods and correction factors for non-Gaussian loads. Comparing the results with results obtained with the rainflow-counting method in the time domain leads to the following main conclusions: It is necessary to use a non-Gaussian correction factor and, if second order wave effects are considered, a spectral fatigue approximation method for widebanded spectra has to be used to get results close to the reference results. It should be noted that wind effects are not considered in the White-Noise approach for this thesis since the focus is on proposing approaches for a quick spectral fatigue assessment with FAST, but not on the detailed estimation of loads.

Keywords: Floating offshore wind turbines, LCOE, FAST, Fatigue, Narrow band approximation, Spectral approximation methods, RAOs, S-N-curve

Acknowledgements

I want to express my gratitude to Professor Wengang Mao for giving me the opportunity to write this thesis and supporting me throughout the work. Our meetings really helped me to better understand how to perform a fatigue assessment in the frequency domain, while his positive feedback kept me motivated. I would also like to thank Xiao Lang for helping me with Python and how to access MetOcean-Data. Furthermore, I want to thank Moritz Gräfe and Wei Yu from the University of Stuttgart for their help and support during the thesis. Their input for the cost model, help with the FAST simulations and also general knowledge about FOWTs has really helped me a lot.

Lastly, I want to thank all my friends and family who have supported me throughout my studies. They did not only contribute to my academic progression but also to my growth as a better person.

Björn Nembach, Gothenburg, June 2022

List of Acronyms

Below is the list of acronyms that have been used throughout this thesis listed in alphabetical order:

AC	Alternating Current
AEP	Annual Energy Production
AHTS	Anchor Handling, Tung and Suppy
BEM	Blade Element Momentum Theory
CAPEX	Capital Expenditures
DC	Direct Current
DECEX	Decommissioning Expenditures
DECOM	Decommissioning
DLC	Design Load Case
D&C	Development and Consenting
FFT	Fast-Fourier-Transformation
FOWT	Floating Offshore Wind Turbines
GEBCO	General Bathymetric Chart of the Ocean
HV	High Voltage
I&C	Installation and Commission
LCOE	Levelized Cost of Energy/Electricity
MBL	Minimum Breaking Load
MoorSys	Mooring System
NBA	Narrowband-Approximation
NTM	Normal Turbulence
NSS	Normal Sea State
OPEX	Operational Expenditures
OW	Operational Weather Window
O&M	Operation and Maintenance
P&A	Production and Acquisition
QTFs	Quadratic Transfer Functions
RAOs	Response Amplitude Operators
RFC	Rainflow-Counting
Substat	Substation
TLP	Tension-Leg-Platform
TLWT	Tension-Leg-Wind-Turbine
TwrBsMyt	Tower Base Bending Moment
WN	White-Noise
WT	Wind Turbine

Nomenclature

Below is the nomenclature of indices, sets, parameters, and variables that have been used throughout this thesis.

Latin letters

A	Area
A_i	Stress caused by a unit wave-induced load
A_w	Scale Parameter
a	Intercept parameter from S-N-curve
C	Costs
D	Damage
d	Water depth
D_i	Inner diameter
D_o	Outer diameter
F	Forces
f	Probability of occurrence
f_z	Zero upcrossing frequency
g	Gravitational constant
H	Transfer function
H_S	Significant Wave height
h	Wave height
h_s	Significant response
I_V	Turbulence intensity
k	Wave number
k_w	Shape parameter
Ku	Kurtosis
L	Distance to nearest coastline

L_{line}	Length of mooring line
M_y	Fore-aft bending moment
m	Wöhler exponent from S-N-curve
m_n	Spectral moments
N	Number of cycles until failure
N_z	Axial Force
n	Number of counted cycles
P	Power
r	Discount rate
S	Sea spectrum
S_{xx}	Power-spectral density
S_{xy}	Cross-spectral density
Sk	Skewness
T	Time
T_m	Average period between local maxima
T_n	Generalized average period
T_w	Wave period
T_p	Peak spectral period
V	Wind speed
W_y	Sectional Modulus

Greek letters

α	Wind shear exponent
α_n	Bandwidth parameters
Γ	Gamma-Function
γ	Correction factor
η	Free-surface profile
ϵ	Steepness
ω	Angular Frequency
λ	Wavelength
Φ	Water velocity potential
σ	Stress

Contents

List of Figures

List of Tables

1
Introduction

Due to climate change the role of renewable energies in the energy system is becoming more important. Wind energy is mostly considered to be one of the most advantageous and effective renewable energy sources because of its low cost and extensive availability. DNV forecasts that the installed capacity of wind energy will reach 1 TW in 2024 and will further increase to 4 TW in 2050, with the share of offshore wind energy being 1.75 TW [1].

Some of the advantages of offshore wind energy compared to onshore wind are that offshore winds are stronger and more reliable, its development needs fewer land resources and the visual and noise impact is less important [2].

Nowadays, mainly fixed offshore wind turbines are installed. These are limited to sites relatively close to the shore due to the water depth. The emerging technology of floating offshore wind turbines enables the access to locations further from the shore with a stronger and more reliable wind resource. The technical feasibility of the technology has been proven by floating wind farms in Scotland and Portugal. The DNV report *Floating offshore wind: The next five years* predicts that by 2050 the share of floating offshore wind will be 15 % of all offshore wind [3].

However, to get there some challenges have to be overcome. One of the main challenges is the financial aspect of FOWTs. While the levelized cost of energy (LCOE) for fixed offshore wind turbines nowadays is below 50 USD/MWh, the LCOE of the first floating wind farms exceeded 200 USD/MWh [3]. The main cost drivers being the turbine and foundation costs, as well as the operational expenditures. With a scale up of the technology and its supply chain the LCOE of floating wind is predicted to drop below 100 USD/MWh by 2025 and 40 USD/MWh by 2050.

Furthermore, FOWTs have to operate in a harsh environment where they have to endure constant loading from wind and waves. In contrast to turbines with a fixed foundation, floating offshore wind turbines are more affected by wave forces due to the movement of the foundation. Over the lifetime of the FOWTs this could lead to cracks forming, growing and in the worst case to failure. Therefore, one of the main challenging tasks for designing FOWTs is to analyze their fatigue damage caused by the combined loads from wind and waves. As FOWTs are typically operated between 20-30 years, its fatigue accumulation is recognized as a high-cycle fatigue problem. The fatigue damage is then estimated by the so-called S-N method based on the linear Palmgren-Miner rule. This can be done in the time or the frequency

domain. In the time domain simulations for defined design load cases are performed to obtain the occurring loads. After calculating the stresses and counting the cycles with a counting-method, the short-term damage is calculated with help of the Palmgren-Miner rule and material parameters form the S-N curve. Several simulations per design load case have to be performed for a complete fatigue assessment, which is computational expensive.

Alternatively, the fatigue assessment can be performed in the frequency domain. With the help of a stress transfer function and the sea spectrum of a sea state the expected short-term fatigue damage can be approximated for every possible sea state. Just a limited number of simulations is necessary to obtain the stress transfer function. Therefore, the spectral fatigue assessment could be used in an early design stage of a FOWT to analyze its fatigue damage for various design load cases with relatively low computational effort, which could speed up the design process.

1.1 Objectives

The objective of this thesis is to take a look at both aforementioned challenges of LCOE and fatigue assessment of FOWTs. The objective in regard to the fatigue assessment is to propose an efficient spectral fatigue assessment method in combination with FAST simulations. The basis of the study is a concept for a tension leg platform, the WindStar TLP system.

With regard to the LCOE the research questions are:

1. What is the LCOE of the WindStar TLP system for a reference case and is it comparable to other concepts?
2. Where are good locations in the North Sea for the WindStar TLP system based on the lowest LCOE?

The research questions for the spectral fatigue assessment are as follows:

1. How can simulations from FAST be used to perform a spectral fatigue assessment?
2. Which spectral approximation method provides the results for short-term damages that are closest to the results of a fatigue assessment in the time domain?
3. Is it necessary to use other correction factors?

1.2 Methodology

In the first part a simple LCOE-model based on capital, operational and decommissioning expenditures, as well as the annual energy production, will be implemented. The LCOE-model will take water depth, distance to the coast and wind resources into account. The goal is to identify areas in the North Sea with a low LCOE. MetOcean-data as an input is therefore necessary to estimate the LCOE in the regarded area.

The second part deals with the spectral fatigue assessment of FOWTs and com-

pares them with the results of the more common method in the time domain. A coupled numerical model for the WindStar TLP system has already been established using the aero-hydro-servo-elastic simulation tool FAST. The model and numerical code will be first used to simulate various combinations of wind and wave loads applied on the FOWT for various working scenarios in the time domain. Then FAST will be used to obtain the stress transfer function. Based on a comparison to the results of the fatigue assessment in the time domain, the spectral fatigue assessment will be evaluated.

2

Literature review and theory

2.1 Floating offshore wind turbine foundations

All floating wind turbine foundation concepts can be categorized into three general classes: spar, semi-submersible and tension leg platform (TLP) structures. The classes are defined by the main method of achieving stability. The three categories are summarized in figure 2.1.

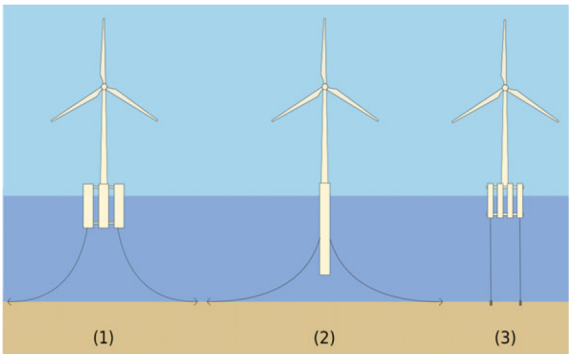

Figure 2.1: Different floater concepts, adapted from [4]

Semi-submersible platforms (1) are buoyancy stabilized. A semi-submersible platform takes advantage of hydrostatic forces of the water plane to ensure stability, while catenary mooring lines are used to anchor the platform to the seabed. One example for a semi-submersible platform is the WindFloat foundation by Principle Power [5].

Spar platforms (2) are ballast stabilized. They are also anchored to the seabed with catenary mooring lines but ensure stability by having a lower center of gravity than center of buoyancy. This is achieved by using ballast weights in the lower part of the cylindrical floater. Examples are the Hywind platform by Statoil or the Sway platform by Sway [6], [7] .

TLPs (3) are mooring line stabilized. The platforms are anchored to the seafloor with taut mooring lines. The tension in the mooring lines results in excellent stability but also high loads on the mooring and anchoring system. An example for a TLP is the Windstar TLP, designed by Zhao et al. [8]. The Windstar TLP system model is used in this thesis. The concept is further explained in chapter 3.

2.2 Environmental Conditions

FOWTs have to operate in harsh environmental conditions. While for a high and reliable energy output it is important to have strong and stable winds, the structure has to endure the loads from wind and waves over its lifetime. Therefore, it is important, both from an economic and technical point of view, to have a good understanding of the environmental conditions a wind turbine operates in.

2.2.1 Wind

In the following section some of the main aspects of how to describe the wind resource will be summarized based on reference [9]. When describing the wind resource, a distinction can be made between deterministic and stochastic wind models. A deterministic model defines the wind field without turbulence with e.g., the mean wind speed and direction, the wind profile over height and deterministic wind gusts. Due to the atmospheric boundary layer and ground friction, the velocity of the wind increases with altitude. The wind profile over height can either be described by the logarithmic wind shear profile or the power law. For this thesis the power law will be used. If the wind speed V_1 at a certain height z_1 is known, the wind speed V_2 at another height z_2 can be calculated with the power law as follows

$$V_2 = V_1 \left(\frac{z_2}{z_1}\right)^{\alpha}, \tag{2.1}$$

where α is the wind shear exponent. Common values for α are between 0.11 and 0.2 [10].

For the description of stochastic wind models another distinction has to be made. On the one hand the long-term statistics with an averaging period over one or several years are important, e.g. for the calculation of annual energy production. On the other hand the short-term statistics with an averaging period of 10 minutes to an hour are important for e.g. fatigue assessment. The long-term wind is composed of a series of short-term wind speeds.

The long-term statistics are described with the (annual) mean wind speed, the distribution function of mean wind speed, e.g. Weibull distribution, and the wind direction distribution. The main statistical parameters to describe the short-term statistics are the (often 10 minutes) average wind speed, the turbulence intensity and a spectral model to describe the turbulence in the frequency-domain. The turbulence intensity is the standard deviation of the wind speed σ_V divided by the mean wind speed V_{mean}

$$I_V = \frac{\sigma_V}{V_{mean}}. \tag{2.2}$$

Common spectral models for the description of the short-term wind in the frequency domain are the Von-Kármán Spectrum [11], Kaimal Spectrum [12] and Mann Spectrum [13].

2.2.2 Ocean Waves

Physics of wave elevation surface

In this section the linear wave theory and stokes second order wave theory will be explained based on [14] and [15]. The three characteristic parameters of a water wave are the wave height H, wavelength λ and water depth d. Additionaly, the wave frequency ω and wave number k are used to describe the kinematics of a single wave in wave theories. The wave frequency and wave number can be calculated by

$$\omega = \frac{2\pi}{T_w}, \tag{2.3}$$

and

$$k = \frac{2\pi}{\lambda}, \tag{2.4}$$

with T_w being the wave period. The wave number and wave frequency are connected via the dispersion relation

$$\omega^2 = g \cdot k \cdot \tanh{(k \cdot d)}. \tag{2.5}$$

For deep waters $k \cdot d$ tends to infinity which results in $\lim_{d\to\infty} tanh(k \cot d) = 1$ and thus in the simplified dispersion relation for deep waters

$$\omega^2 = g \cdot k. \tag{2.6}$$

The simplest wave theory is the linear, regular wave theory. It is based on the potential flow theory. The water's velocity potential ϕ on the water surface (z=0) must satisfy the linearized free-surface boundary condition in equation (2.7). The condition states that at the water surface the water pressure has to be equal to the atmospheric pressure on the free surface and fluid particles must have the same vertical velocity as the free surface.

$$\left[\frac{\partial^2 \phi}{\partial t^2} + g\frac{\partial \phi}{\partial z}\right]_{z=0} = 0. \tag{2.7}$$

In case of linear, periodic waves one possible solution for this condition is

$$\phi = \frac{H}{2}\frac{g}{\omega}e^{kz}\sin{(\omega t - kx)} \tag{2.8}$$

From eq. 2.8 the wave free-surface profile η of a linear, regular wave can be derived

$$\eta_1(t, x) = \frac{H}{2}\cos{(\omega t - kx)}. \tag{2.9}$$

Other wave theories like the Stokes second-order wave theory add a correction to the linear wave theory to account for non-linear effects. This results in a more accurate

model for real surface waves. According to Stokes the non-linear wave profile with second order wave correction can be described by the power series

$$\eta(x,t) = \epsilon^1 \cdot \eta_1(x,t) + \epsilon^2 \cdot \eta_2(x,t), \tag{2.10}$$

where $\epsilon = k \cdot H/2$ is the steepness and η_2 the second-order Stokes correction

$$\eta_2(x,t) = k \left(\frac{H}{2}\right)^2 \frac{\cosh(kd)}{4sinh^3(kd)} (2 + \cosh(2kd)) \cos(2(\omega t - kx)). \tag{2.11}$$

This enables the modelling of more realistic waves with steeper wave crests and flatter wave troughs. The combination of a linear wave with second-order Stokes correction can be seen in figure 2.2.

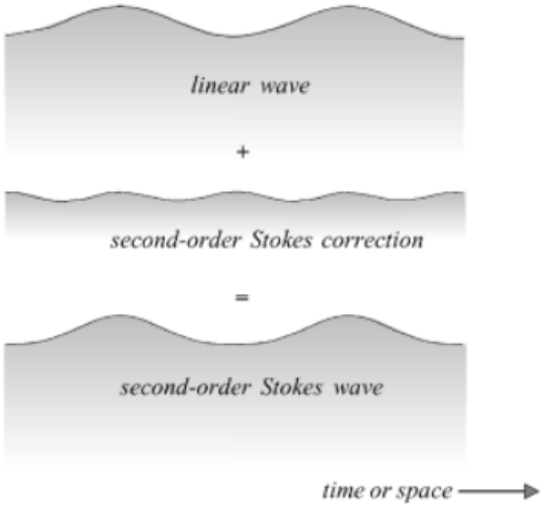

Figure 2.2: Surface profile of a second-order Stokes wave [15]

Irregular (stochastic) waves

An irregular random wave is described with the help of a wave energy density spectrum of a sea state. The spectrum defines the wave's energy content and its distribution over the wave's frequency range [16]. The wave free-surface profile in the time-domain can be obtained by discretizing the spectrum in frequency intervals, determining the amplitude of each interval, assigning a random phase and then summing up the single waves, see figure 2.3 [17]. The most important statistical parameters to describe a sea state are the significant wave height H_s, peak spectral period T_p and wave standard deviation σ. The significant wave height is defined as the average height of the highest third of waves and can be calculated with

$$H_s = 4\sigma. \tag{2.12}$$

The peak spectral period is related to the peak frequency $\omega_p = 2\pi/T_p$, at which the spectrum has its peak.

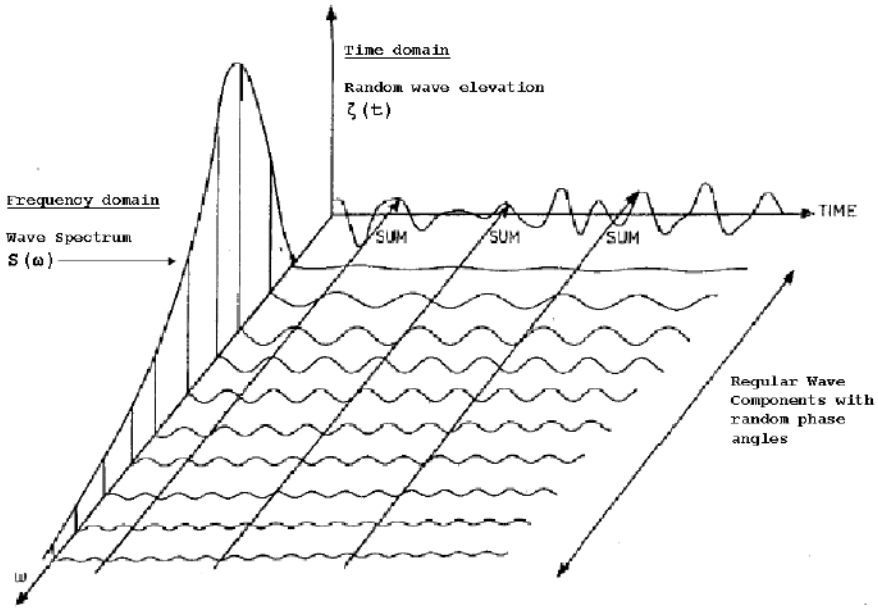

Figure 2.3: Connection between wave spectrum and random wave elevation in the time domain [17]

The most commonly used spectrum formulas for the description of sea states are the Pierson-Moskowitz (P-M) [18] and JONSWAP [19] model. The JONSWAP-Spectrum is a modification of the Pierson-Moskowitz-Spectrum to better describe a not fully developed sea state.

Pierson-Moskowitz-Spectrum:

$$S(\omega) = \frac{\alpha g^2}{\omega^5} \exp\left(-\frac{5}{4}\left(\frac{\omega}{\omega_0}\right)^{-4}\right) \tag{2.13}$$

JONSWAP-Spectrum:

$$S(\omega) = \frac{\alpha g^2}{\omega^5} \exp\left(-\frac{5}{4}\left(\frac{\omega}{\omega_0}\right)^{-4}\right) \gamma^{\exp\left(\frac{-(\omega-\omega_p)^2}{2\sigma^2\omega_p^2}\right)} \tag{2.14}$$

The scale parameter α and peak shape parameter γ depend on the significant wave height and peak period.

2.3 Costs for FOWTs

The levelized cost of electricity is a useful metric to decide between different alternatives for energy production. It puts the total life-cycle costs in relation to the produced energy, discounted to a given date. The life-cycle costs consist of different

investment expenses and operation and maintenance costs. According to the International Renewable Energy Agency (IRENA) [20], the LCOE can be calculated with

$$LCOE = \frac{\sum_{t=1}^{n} \frac{I_t + M_t + F_t}{(1+r)^t}}{\sum_{t=1}^{n} \frac{E_t}{(1+r)^t}}, \tag{2.15}$$

where in case of wind energy the fuel consumption F_t is

$$F_t = 0 \tag{2.16}$$

In eq. (2.15), I_t are the investment expenses at time t, M_t the operation and maintenance costs at time t, E_t the energy generation at time t, and r the discount rate.

The life cycle costs and LCOE of offshore wind farms and FOWTs have been studied quite a lot in literature. *Ioannou et al.* [21] developed a life-cycle techno-economic model for an offshore wind farm. *Castro-Santos et al.* [4] described a general model to estimate the costs of an offshore wind farm. This model was applied to the coast of Galicia in Spain to see how the costs are affected by the distance to the shore and water depth. *Myhr et al.* [22] developed a model for the LCOE of different kinds of FOWTs, based on [23]. One of their main conclusions was that the costs are strongly dependent on water depth and the distance to the shore, due to an increase of mooring costs and export cable length.

All of the different studies divide the life cycle costs into different phases. According to reference [22] these are:

1. Development and consenting: Includes designing and development of the project.
2. Production and acquisition: The necessary components are produced or aquired from external sources.
3. Installation and commissioning: The components of the project are installed.
4. Operation and maintenance: The wind turbine/farm is operating and has to be maintained to ensure its availability.
5. Decommission: The turbine/farm has reached its end of life and its components are dismantled.

The investment expenses, also called CAPEX for capital expenditures, occur during phases 1, 2 and 3. The operating and maintenance expenditures (OPEX) occur in phase 4, while the decommissioning expenditures occur in phase 5.

2.3.1 Annual energy production

Furthermore, phase 4 is the phase in which electricity is generated. If the wind speed distribution at hub height and the wind turbine's power curve is known, the gross annual energy production AEP can be calculated with the following formula [10]:

$$AEP = t_{annual} \sum_{i=1}^{N_v} f(v_i) P(v_i), \tag{2.17}$$

where t_{annual} is the number of hours per year, $f(v_i)$ the probability of occurence for the wind speed bin v_i and $P(v_i)$ the power output of the wind turbine at wind speed v_i, taken from the power curve.

The net annual energy production takes losses in account, too. The main losses of a wind farm are due to wake effects, downtimes, electrical issues, turbine performance issues, environmental issues, like e.g ice on the blades, and curtailment [10].

2.4 Aero-hydro-servo-elastic modelling

A commonly used software to simulate the dynamic response of a wind turbine and its (floating) foundation is FAST, developed by the US National Renewable Energy Laboratory (NREL) [24]. FAST works with several modules. For example, AeroDyn calculates aerodynamic loads, HydroDyn calculates hydrodynamic loads and FEAM calculates loads on the mooring system.

The loads on the structure are needed to solve the time-domain dynamic equation motion of the whole system, which can be expressed as [25]

$$\mathbf{M}_{ij}(\eta, u, t)\ddot{\boldsymbol{\eta}}_j = \mathbf{F}_i(\eta, \dot{\eta}, u, t) \tag{2.18}$$

with the (i,j) component $\mathbf{M}_{ij}$ of the inertia matrix of the entire system, the system acceleration $\ddot{\boldsymbol{\eta}}_j$ and the forces or moments on the system $\mathbf{F}_i$. $\mathbf{M}_{ij}$ is dependent of the system displacement η, control input u and time t. The indices i, j are associated with the degree of freedoms of the system.

The six degrees of freedom related to the floating structure of the system are sway, surge, heave, pitch, roll and yaw, see figure 2.4.

2.4.1 Aerodynamic load modelling

FAST uses the blade element momentum (BEM) theory to model the aerodynamic loads on the blades of the wind turbine [27]. The two main assumptions of the BEM are that the rotor is assumed to be an actuator disk in a stream tube and the forces at the local blade element are equal to the forces from a global momentum balance. To get a more realistic model different correction models can be added to the BEM. In this study, Prandtl's tip loss factor corrects the effect of blade tip and hub losses. Dynamic stall is corrected with the semi-empirical Beddoes-Leishman correction [28].

2.4.2 Hydrodynamic load modelling

The hydrodynamic model used in FAST is based on the potential flow theory. The hydrodynamic forces on a floating structure consist of the hydrodrostatic restoring force F_i^{hys}, wave-radiation force F_i^{rad}, wave-exciting force F_i^{exc} and the non-linear

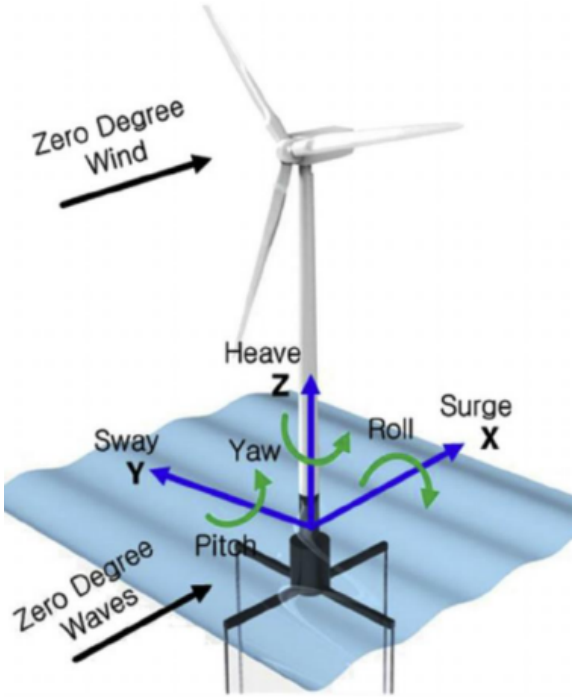

Figure 2.4: The six DoF of a floating structure [26]

viscous drag force F_i^{vis} [25]

$$F_i^{hydro} = F_i^{exc} + F_i^{hys} + F_i^{rad} + F_i^{vis}. \tag{2.19}$$

The wave excitation force acts on the fixed, not moving platform. The first order wave excitation force results from Froude-Kriloff and diffraction forces [29]. If second order wave forces are considered, the full difference- and sum-frequency quadratic transfer functions (QTFs) are needed. Dependent on the QTFs, the second-order terms are then calculated by using the first-order wave amplitudes and adding extra energy to the wave spectrum [30].

For the radiation force the water is assumed to be still while the platform is forced to oscillate. These radiation effects result from acceleration dependent added mass, velocity dependent radiation damping and buoyancy restoring forces [29].

The non-linear viscous drag force is assumed to be the viscous term of the Morison's equation [25].

The hydrodynamic coefficients such as the added mass, damping, wave exciting linear transfer function and QTFs are calculated by frequency-domain hydrodynamic panel codes like WADAM [31].

2.4.3 Mooring line load modelling

The tendons are modelled with the elastic rod model which takes mooring inertia and drag forces into account [32]. The two governing equations of the rod model

are the equation of motion

$$\rho_w \ddot{\mathbf{r}} + C_a \rho_w \ddot{\mathbf{r}}^n + (EI\mathbf{r}'')'' - (\tilde{\lambda}\mathbf{r}')' = \tilde{\omega} + \overline{\mathbf{F}_r}^d \tag{2.20}$$

and, assuming a small, linear stretch of an extensible rod, the stretch condition of $\mathbf{r}$

$$\frac{1}{2}(\mathbf{r}' \cdot \mathbf{r}' - 1) = \frac{T}{A_r E} \approx \frac{\lambda}{A_r E}. \tag{2.21}$$

The rod's position vector $\mathbf{r}(s,t)$ is a function of the rod arc length s and time t, ρ_w is the density of water, EI the bending stiffness, $\tilde{\lambda}$ a scalar function related to tension and curvature of the rod, $\tilde{\omega}$ the rod's wet mass and $\overline{\mathbf{F}_r}^d$ the hydrodynamic force [33]. Equations (2.20) and (2.21) are non-linear and therefore solved with the finite element method.

2.5 Structure stress response

Response amplitude operators (RAOs)

Response amplitude operators, also known as transfer functions, are commonly used in offshore engineering to describe the wave induced motions or loads on a structure in the frequency domain. Simply put, the transfer function $H(\omega)$ is the ratio of the response to the input wave height over the frequency spectrum. A common way to calculate the transfer functions for a linear response is by simulating the response to regular waves at different wave frequencies and calculating the ratio of the response amplitude Y to the wave input amplitude X

$$H(\omega) = \frac{Y(\omega)}{X(\omega)}, \tag{2.22}$$

The wave input amplitude $X(\omega)$ of a regular wave can be described with its wave height H

$$X = \frac{H}{2}. \tag{2.23}$$

Another way to calculate the RAOs with FAST was proposed by NREL in [34]. A white-noise spectrum is used to describe the time-domain wave excitation and FAST computes the loads on the turbine. Six sets of simulations with different random seeds are carried out and the responses are averaged. After calculating the power-spectral density $S_{xx}(\omega)$ of the input (wave elevation) and the cross-spectral density $S_{xy}(\omega)$ of the input/output (load response) the RAO can be computed as follows:

$$H(\omega) = \frac{S_{xy}(\omega)}{S_{xx}(\omega)}. \tag{2.24}$$

The power-spectral density S_{xx} of a signal describes its power distribution over a frequency range. The cross-spectral density S_{xy} describes the relation between the output and input signal [35].

Once the load transfer functions H_i, e.g the axial force and horizontal bending moment, are known the stress transfer function can be expressed by

$$H_\sigma(\omega) = \sum_i A_i H_i(\omega), \tag{2.25}$$

where A_i is the stress caused by a unit wave-induced load.

Structure stress response spectrum

There are two ways to calculate the stress response spectrum in a sea state. If the stress response in the time-domain is known, the stress response spectrum is calculated by performing a Fast Fourier Transformation of the stress time series and calculating the power-spectral density. Alternatively, the stress transfer function $H_\sigma(\omega)$ and the spectrum of the sea state $S(\omega|H_s, T_p)$ need to be known. Because the transfer function describes the relation between stress response and wave input, the stress response spectrum can be estimated by combining the stress transfer function with the wave spectrum

$$S_\sigma(\omega|H_s, T_p) = |H_\sigma(\omega)|^2 S(\omega|H_s, T_p). \tag{2.26}$$

This equation is valid for a single heading angle. For more than a single heading angle the transfer function is dependent on the heading angle. Therefore, equation 2.26 would also be dependent on the heading angle [36].

2.6 Fatigue Damage

Cyclic loading over time results in fatigue damage. The damage of a single cycle is insignificant but with an increasing number of cycles a crack may form, grow and then lead to failure of the considered component. If the number of cycles exceed 10^4 cycles to failure it is called high cycle fatigue. The material performance for high-cycle fatigue is characterized by the S-N-curve of the material, which is obtained by experimental fatigue tests. The S-N-curve shows on a logarithmic scale how many cycles N per stress range $\Delta\sigma_s$ a material can endure until failure. The basic design S-N curve is [37]:

$$\log N = \log a - m \log \Delta\sigma_s, \tag{2.27}$$

where $\log a$ is the intercept of the logarithmic N-axis by the curve and m the negative inverse slope of the S-N-curve, also called Wöhler exponent. Typical S-N-curves can be found in DNV guidelines like in references [37] or [36]. Figure 2.5 shows three S-N-curves for C-Mn steel. Curve I is the S-N-curve of a welded joint and curve III of the base material in air with cathodic protection. Curve IV is the S-N-curve of the base material in a corrosive environment. These S-N-curves are only applicable

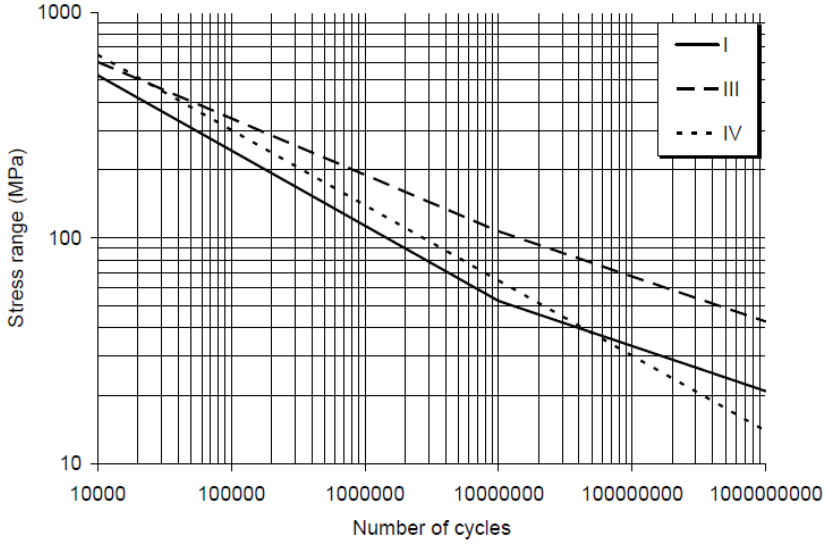

Figure 2.5: S-N-curves for C-Mn steel (I, III, IV) [36]

for rolled or extruded plates and flats [36].

The loads on mechanical components are usually a complex series of random loads of different sizes which makes it difficult to count the number of cycles per stress range in the time domain. The most common approach to count the number of cycles is the Rainflow-counting-method (RFC). RFC is generally seen as the most accurate counting method. The basic idea of the algorithm can be explained as follows. The plot of a continuous stress time series is rotated by 90° and the local minima and maxima are connected with straight lines. The next step is to imagine rain drops running down the slopes, starting from every local maximum and minimum. If one of the following conditions is met the drop "stops" and is counted as a half cycle with a magnitude equal to the stress difference between its start and termination:

- The drop is originated from a minimum and passes a minimum of at least the same size
- The drop is originated from a maximum and passes a maximum of at least the same size
- The drop reaches the running path of another drop

Half cycles starting at local maxima are paired together with half cycles of the same magnitude starting at local minima to form full cycles with a stress range $\Delta\sigma_s$.

When the number of cycles per stress range $n_i(\Delta\sigma_s^i)$ are known the fatigue damage can be calculated according to Palmgen-Miners linear damage accumulation rule:

$$D = \sum_i \frac{n_i}{N_i} \tag{2.28}$$

With the number of cycles until failure N_i from the S-N-curve, see equation (2.27), the damage within the time series can be calculated with

$$D(T) = \sum_i \frac{n_i \Delta(\sigma_s^i)^m}{a} \tag{2.29}$$

The probability of failure increases with increasing damage. For design purposes the failure criteria at which the failure is assumed to occur is

$$D_{failure} = 1. \tag{2.30}$$

Alternatively, the expected short-term fatigue damage can be estimated in the frequency domain. Here, the stress response spectrum needs to be known to estimate the damage with by means of spectral approximation methods. For narrow-banded, stationary, Gaussian loads the narrow-band approximation gives reasonably good estimations for the expected damage but the response spectrum of practical engineering structures is often not exactly narrow-banded and Gaussian [38]. Therefore, correction methods for wide band properties and non-Gaussianity can be used to improve the approximation of the expected damage [39]. Different spectral approximation methods for widebanded spectra have been proposed, among others, by *Sakai and Okamura* [40], *Jiao and Moan* [41], *Benasciutti and Tovo* [42], *Wirsching and Light* [43], *Dirlik* [44] and *Zhao and Baker* [45]. More details about the wideband correction methods can be found in reference [46].

The spectral approach with narrow-band approximation plus Dirlik and Zhao-Baker correction has been studied by *Adilah et al.* for a semi-submersible FOWT under combined wind and wave loads [47]. They used a numerical in-house tool called NK-UTWind to simulate the response of a FOWT. In this study the Dirlik correction showed the best results compared to the rainflow-counting reference damage.

The different methods for correction factors for a non-Gaussian load distribution are based on the Skewness and Kurtosis of the distribution. For a Gaussian distribution the Skewness and Kurtosis are 0 and 3, respectively. Thus, the difference to those values can be used as a measure for non-normality [39]. A common non-Gaussianity correction method is the correction according to *Winterstein* [48]. Another correction method was proposed by *Braccesi and Cianetti* [39].

3
Windstar TLP Model

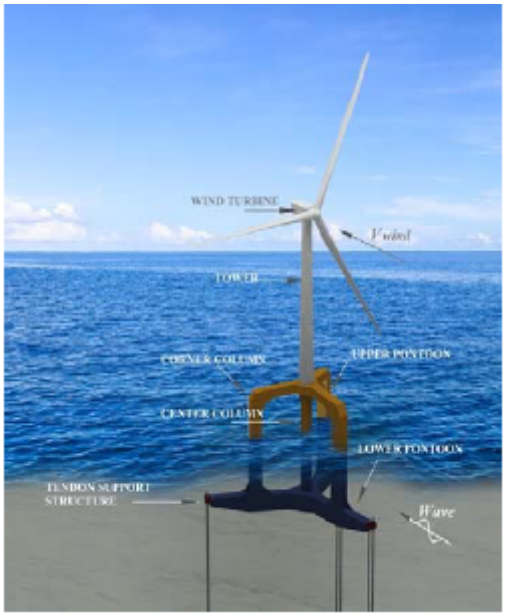

Figure 3.1: Windstar TLP system [49]

The whole Windstar TLP system is an assembly of the floating foundation, a tower and a NREL 5 MW offshore wind turbine [50].
The Windstar TLP floating foundation consists of one central column with three radial columns, pontoons and tendon support structures [8], see figure 3.1. The three radial columns provide external stabilisation during operation and allow the system to be towed for transportation.
A pair of polyester tendons is attached to each tendon support structure and anchored to the seabed with a gravity anchor [28].
The tower is placed on the center column and the NREL 5 MW offshore wind turbine is a horizontal aligned, upwind, blade-pitch-controllable wind turbine [50].
The main model properties of the wind turbine and the entire WindStar TLP system can be seen in tables 3.1 and 3.2, respectively.

The WindStar TLP system was designed by *Zhao et al.* in 2012 [51][8]. In further studies its coupled dynamic response for wind-only, wave-only and the combined wind and wave case has been studied [28][31]. An experimental study of the system was conducted in 2018 to obtain viscous drag coefficients [52]. Furthermore, *Xie et al.* [53] studied the prediction of springing-induced extreme responses of the

Property	Value	Unit
Rotor diameter	126.0	m
Cut-in wind speed	3	m/s
Rated wind speed	11.4	m/s
Cut-out wind speed	25	m/s
Rated rotor rotational speed	12.1	rpm
Rotor mass	110 000	kg
Nacelle mass	240 000	kg

Table 3.1: Model properties of the NREL 5MW wind turbine [50]

Property	Value	Unit
Design draft	30	m
Centre column diameter	4.5	m
Distance between the centre column and corner column	20.8	m
Vertical centre of mass	34.17	m
Total displacement	5466.0	t
Tower base outer diameter	5.6	m
Tower base thickness	50	mm
Roll moment of inertia	1 142 000	$t \cdot m^2$
Pitch moment of inertia	1 142 000	$t \cdot m^2$
Yaw moment of inertia	1 373 000	$t \cdot m^2$
Surge/Sway natural frequency	0.022	Hz
Heave natural frequency	0.27	Hz
Roll/Pitch natural frequency	0.22	Hz
Yaw natural frequency	0.038	Hz
Pretension	2370	t
Tendon diameter	227	mm
Weight in air	35.4	kg/m
Axial stiffness	391.0	MN
Radius of fairlead	40.7	m

Table 3.2: Main parameters of the WindStar TLP system [49]

tendons. The system's transient response to tendon failure was studied by *Wu et al.* [33] and *Liu et al.* [49] studied the effect of second-order wave forces on fatigue damage assessment of the system. They concluded that the second order waves have a dominant effect on the tower's structural damage.

All of the numerical studies have been performed for an assumed installation site of the WindStar TLP system at 61°20' N latitude and 0°0' E longitude, which is near the Shetland Islands, northeast of Scotland [8]. The site was also basis for a load analysis for another type of FOWT performed by *Jonkman et al.* [25] and was chosen because of its fairly extreme wind and wave conditions. Therefore, if the results of the stress analysis or fatigue assessment carried out are positive, the FOWT can be used for almost any site.

3.1 Design Load Cases and simulation setup

The design load cases (DLCs) for this location used in the previously mentioned studies have been determined according to the IEC 61400-3 standard [54]. The standard specifies how design load cases for all possible situations during the turbine's life, e.g. normal operations and emergencies are determined. The DLCs must cover a wide range of combinations of wind and wave conditions. The wind conditions are defined by using wind speed bins. The IEC standard suggests a bin size of 1.4 m/s. The wave conditions are defined by the expected significant wave height H_s and peak spectral period T_p for the respective wind speed bin. The expected values are found by investigating the joint distribution of wind and wave data [25]. The used site-specific DLCs for a wind turbine under operating conditions are summarized in table 3.3. A normal turbulence model (NTM) is used for the wind and a normal sea state model (NSS) for the waves.

An already existing FAST model of the WindStar TLP system is used to perform the simulations required to estimate the short-term damage in the time domain as a reference, as well as simulations necessary for the spectral fatigue assessment. A minimum length of simulation of 10-minutes is recommended by the IEC 61400-3 standard to perform a fatigue analysis in the time domain for onshore and fixed offshore wind turbines [54]. However, the DNV-guideline DNVGL-ST-0119 suggests using simulations with a minimum of 3 hours for FOWT certification to adequately capture nonlinear and second-order wave effects [55]. For this thesis, however, a simulation length of one hour is chosen, which is regarded as sufficient for research purposes. The total simulation time for time-domain simulations within this thesis is set to 3630 seconds with the first 30s cut off before post-processing to mitigate transient effects. Furthermore, the IEC 61400-3 standard recommends that it is necessary to perform at least six simulations with different random seeds for each combination of turbulent wind and stochastic wave conditions [54].

The turbulent wind fields are generated using the Kaimal spectral model in TurbSim. As it is computationally expensive to generate turbulent wind fields with a length of one hour, repeating periodic wind files can be used [56]. In this thesis, the

DLCs	Wind conditions		Wave conditions			Turbine status
	Model	V [m/s]	Model	H_s [m]	T_p [s]	
1	NTM	4.2	NSS	1.6	11	Operating
3	NTM	5.6	NSS	1.8	11.2	Operating
3	NTM	7.0	NSS	1.8	11.1	Operating
4	NTM	8.4	NSS	2.0	10.9	Operating
5	NTM	9.8	NSS	2.2	10.9	Operating
6	NTM	11.4	NSS	2.4	10.9	Operating
7	NTM	12.6	NSS	2.7	11.2	Operating
8	NTM	14.0	NSS	3.0	11.4	Operating
9	NTM	15.4	NSS	3.4	11.8	Operating
10	NTM	16.8	NSS	3.7	12.0	Operating
11	NTM	18.2	NSS	4.1	12.3	Operating
12	NTM	19.6	NSS	4.4	12.7	Operating
13	NTM	21.0	NSS	4.7	12.8	Operating
14	NTM	22.4	NSS	5.2	13.3	Operating
15	NTM	23.8	NSS	5.5	13.5	Operating

Table 3.3: Definitions of design load cases, adapted from [49]

wind field is assumed to repeat itself after 10 minutes.

The simulation of wave loads is handled within the HydroDyn module of FAST. For all simulations a Pierson-Moskowitz sea spectrum is assumed.

3.2 Load Validation

To ensure that the FAST simulations were set up correctly and the load time series can be used to estimate the short-term fatigue damage, the simulations are validated. They are validated by comparing the statistical properties of the tower base bending moment TwrBsMyt of the performed simulations with the statistical properties found in [49]. The statistical properties for each DLC are calculated by calculating the mean of the respective statistical parameter over the six simulations performed per DLC. The regarded statistical properties are the mean, maximum, minimum and the 97.5th quantiles. The reference values for the first (cut-in), sixth (rated) and last (cut-out) DLCs can be seen in figure 3.2. The figure includes the statistical properties for the cases wind only, first order wave effects only, first and second order wave effect, first order waves with wind and wind plus first and second order wave effects. Note that the description of the boxplots in the bottom left corner of figure 3.2 contains an error as the values shown are the 97.5th quantiles instead of the mean plus/minus standard deviation. The statistical properties of the simulations performed within this thesis for the first, sixth and last DLCs are summarized in figure 3.3. Here, the cases where only wind and first order wave effects with wind occur are disregarded.

The mean values of the performed simulations for the tower base bending moment are the same as in the reference. This is also true for the 97.5th percentile points. Slight differences can be observed for the minimum and maximum values. For example the maximum of the WindWave^{2nd} is close to 110 MNm in the performed simulations while it is 105 MNm in the reference. These differences can be attributed to the use of different random seeds for wind and waves in the simulations.

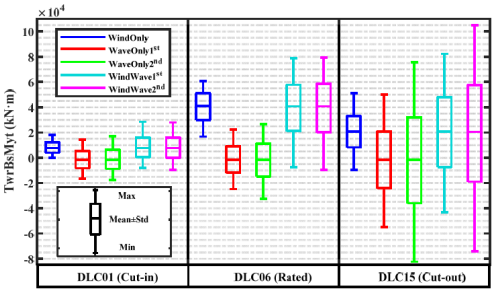

Figure 3.2: Statistical properties of TwrBsMyt for DLC1, 6&15 from reference [49]

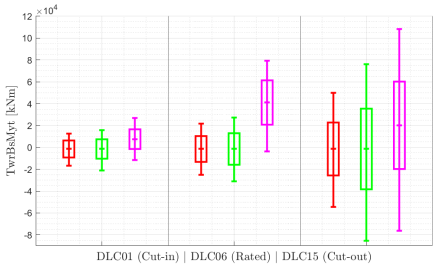

Figure 3.3: Statistical properties of TwrBsMyt for DLC 1, 6&15 from simulations performed in this thesis

Due to the similar statistical properties as in the reference, it can be concluded that the simulations were carried out correctly and the load time series can be used for the calculation of the stresses and fatigue damage in the time domain.

4
LCOE model

The goal for this chapter is to find a relatively simple cost model that can estimate the LCOE for the Windstar TLP system at different locations based on MetOceanData. *Myhr et al.* [22] concluded in a sensitivity analysis of their model that the water depth, the distance to the shore and capacity factor are the most significant factors for the LCOE of FOWTs. Therefore, those parameters will be variable in the model and later derived from MetOceanData. The water depth and the distance to the shore will be noted as d and L, respectively. The influence of the capacity factor is included in the calculation of the annual energy production, which depends on the wind resource at the location and the wind turbines power curve.

The LCOE-model is based on the reference base-case model used by *Myhr et al.* [22] and *Bjerkseter and Ågotnes* [23] but adapted for the WindStar TLP system. As a project with just a single wind turbine is unrealistic it was decided to assume a wind farm of 100 turbines for the LCOE-model. This corresponds to an installed capacity of 500 MW. Other main assumptions that were adopted from *Myhr et al.* [22] are summarized in table 4.1. The fuel cost for vessels needed for installation,

Years for development	5
Years of operation	20
Number of turbines	100
Installed capacity	500 MW
Wind farm availability	93.80%
Wake effect losses	7%
Electric array losses	1.80%
Other losses	3%
Price for Marine quality treated S355 steel	1000 €/ton

Table 4.1: Main assumptions for the LCOE-model, from [22]

operation and management and decommission is assumed to be included in their daily rates. The daily rates for the different vessel types can be found in table 4.2. A detailed explanation of the different vessels and a discussion of the costs was done by *Bjerkseter and Ågotnes* [23].

Vessel Type	Costs [k€/day]
Crane vessel	531
Inshore crane barge	55
Anchor handling, tug and supply (AHTS)	91
Tug boat	17
Onshore mobile crane	6

Table 4.2: Approximate day-rates of different vessels, including mean fuel consumption, adapted from [23]

The LCOE-model will be divided into five modules, that include the respective life phases from section 2.3, see figure 4.1.

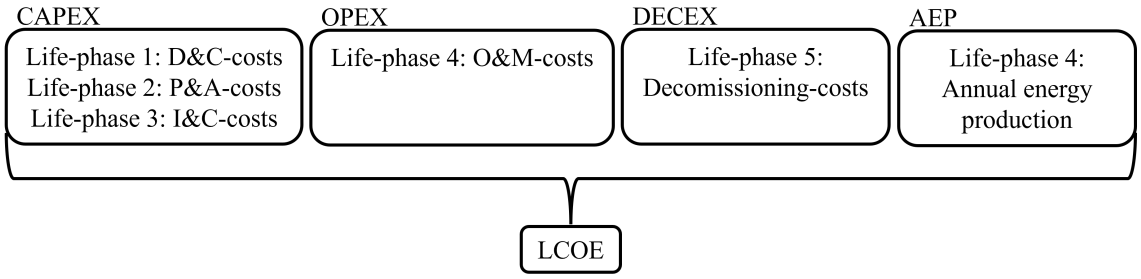

Figure 4.1: The five modules of the LCOE-model

The final model will use water depth and distance to the shore from MetOcean-Data as input for the calculation of costs for different locations. Furthermore, it will use wind speed data as input to calculate the annual energy production. The MetOcean-Data sets used in this thesis are discussed in the following section.

4.1 MetOcean Data

To get the water depth at different locations the General Bathymetric Chart of the Ocean (GEBCO) data from 2020 [57] can be used. The GEBCO Grid provides elevation data of the seabed surface in negative meters on a 15 arc-second interval grid using the mean sea level as reference. For a finer resolution the elevation is interpolated between the grid points.

The dataset "Distance to Nearest Coastline" on a 0.1 degree grid of northern latitude and eastern longitude created by NASA's Ocean Biology Processing Group (OBPG) and published by the Pacific Islands Ocean Observing System (PacIOOS) was used to get the distance to the closest shore for the North Sea area [58].

To get the wind speed on a 0.1 degree grid ERA5 re-analysis data [59] can be used. The ERA5-reanalysis dataset provides hourly estimates for many important

climate and oceanic variables. For this thesis the neutral wind speed with zonal and meridional components at 10 meters u_{10} and v_{10}, respectively, were selected over a period of 6 years from 2016-2021. Based on the neutral wind the actual wind speed can be calculated with

$$V_{10} = \sqrt{u_{10}^2 + v_{10}^2}. \tag{4.1}$$

When the actual wind speed at 10 meters is known, the wind speed at hub height can be calculated with the power law, see equation (2.1). For this thesis a vertical power-law shear exponent $\alpha = 0.14$ was used at every grid point. The same power-law coefficient was used by *Jonkman* [25] to determine the environmental conditions on which previous WindStar TLP studies are based on.

4.2 Annual energy production

To calculate the annual energy production the wind speed distribution and power curve of the wind turbine are needed. In this thesis the design power curve of the NREL 5MW offshore wind turbine [50] is used. The power curve can be seen in figure 4.2.

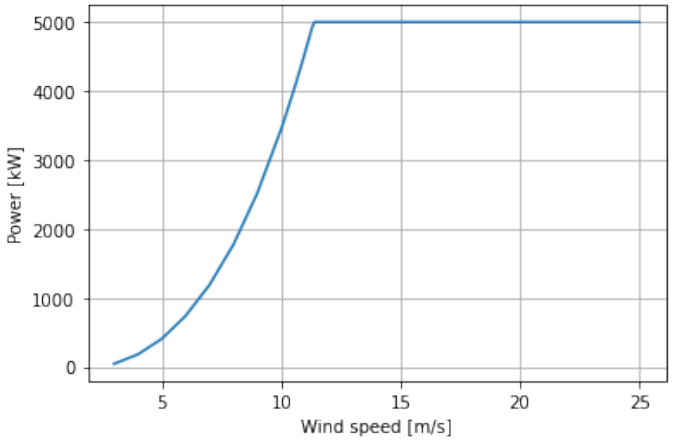

Figure 4.2: Power curve of the NREL 5MW offshore wind turbine [50]

The wind speed distribution can be estimated by fitting the hourly wind speed data at each grid point to a Weibull distribution. A Weibull distribution has the form

$$f(V) = \frac{k_w}{A_w}\left(\frac{V}{A_w}\right)^{k_w-1} e^{-\left(\frac{V}{A_w}\right)^{k_w}}, \tag{4.2}$$

where A is the scale parameter which is closely related to the wind speed and k the non-dimensional shape parameter. To account for yearly changes in the distribution this was done per year. Figure 4.3 shows a histogram of the wind speed distribution at 61°20' N latitude and 0°0' E longitude together with the fitted Weibull probability function for the year 2016. The scale and shape parameters for this case are 12.63

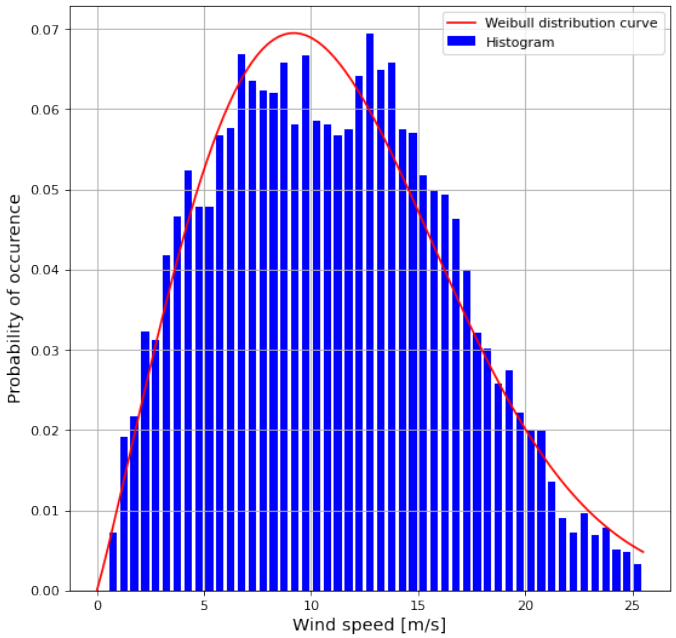

Figure 4.3: Histogram of wind speed distribution with fitted Weibull distribution for 61°20' N latitude and 0°0' E longitude.

and 2.07, respectively.

With the power curve as a function $P(V_i)$, the estimated wind speed frequency distribution $f(V_i)$ and the number of hours in a year, the annual energy production for each year can be calculated with equation (2.17). The LCOE model uses the average annual energy production over the considered five years.

4.3 CAPEX

The capital expenditures, depending on water depth and distance to the shore can be formulated as

$$C_{CAPEX}(d, L) = C_{TotalD\&C} + C_{P\&A}(d, L) + C_{I\&C}(d, L) \tag{4.3}$$

The calculation of the three terms on the right hand side are explained in the following sections.

4.3.1 Costs for Development and Consenting

The development and consenting costs $C_{D\&C}$ for a wind farm with 500 MW installed capacity can be estimated as 104.000 k€ [23]. Another cost that is attributed to the first life-phase is the cost for a construction phase insurance, which is estimated to be 50 k€ per MW [23]. The total costs for the first life-phase are

$$C_{TotalD\&C} = C_{D\&C} + C_{Ins} \tag{4.4}$$

4.3.2 Costs for Production and Acquisition

The costs for production and acquisition include the manufacturing and production costs of the tower and turbine C_{WT}, the floating substructure $C_{Floater}$, the mooring lines C_{Moor}, the anchor C_{Anchor} and the acquisition costs for the inter-array and export cables C_{Cables} and the offshore and onshore substations $C_{Substat}$

$$C_{P\&A}(d, L) = C_{WT} + C_{Floater} + C_{Moor}(d) + C_{Anchor} + C_{Cables}(d, L) + C_{Substat} \quad (4.5)$$

The cost for a single wind turbine is estimated to be approximately 7475 k€ [22]. This includes the tower.

The costs for production and manufacturing of the floating substructure can be calculated as follows [22]

$$C_{Floater} = C_{Material} + C_{Manufacturing}, \quad (4.6)$$

where the manufacturing costs are described with help of a complexity factor which takes the difficulty of manufacturing into account

$$C_{Manufacturing} = \alpha_{complex} \cdot C_{Material}. \quad (4.7)$$

The Windstar TLP's hull is made of wielded, high tensile steel and weighs 1950 tons [8]. By comparing the WindStar TLP concept with the concepts studied by *Myhr et al.* a complexity factor of $\alpha_{complex} = 150\%$ was chosen. This is lower than the WindFloat and higher than the TLWT complexity factors, which are 200% and 130%, respectively [22].
The production costs for a single WindStar TLP substructure can then be estimated to be about 4875k€.

The production costs of the mooring lines depend on the mooring line length L_{line} and therefore on the water depth. The WindStar TLP system uses 3 pairs of polyester mooring lines with a minimum breaking load (MBL) of 17.26 MN. The costs for a polyester mooring line can be estimated with the following formula [60]

$$C_{polyester}(MBL, L_{line}) = (0.0138 \cdot MBL + 11.281) \cdot L_{line}, \quad (4.8)$$

with the minimum breaking load MBL in kN. Because it is a taut mooring system it is assumed that the mooring line length is proportional to the water depth. According to the existing FAST model of the system the unstretched mooring line length at 160 m water depth is 132.23 m [49] . The line length dependent on water depth is then formulated as

$$L_{line}(d) = \frac{132.23}{160} \cdot d. \quad (4.9)$$

The assumptions for the mooring lines made above result in a total cost of the mooring lines for a single Windstar TLP system of

$$C_{Moor}(d) = 6 \cdot (0.0138 \cdot MBL + 11.281) \cdot \frac{132.23}{160} \cdot d. \quad (4.10)$$

The WindStar TLP system is anchored to the seabed with three gravity anchors, each connected to a pair of tendons [28]. For simplicity it is assumed that the gravity anchors are blocks of concrete. Assuming the density of normal weight concrete is about 2400 kg/m^3 [61] the mass and volume of a single concrete anchor can be calculated with help of archimedes principle, see Appendix A. By assuming a price of 41 € per ton of concrete [62] and using equation (4.6) with an complexity factor of 0.5, the production costs for a single anchor are approximately 12300 €.

Two different kinds of cables are necessary for a wind farm. The inter-array cables connect the wind turbines with each other and to the offshore substation and the export cable connects the offshore substation with the onshore substation.

$$C_{cables}(d, L) = C_{inter-array}(d) + C_{export}(L) \tag{4.11}$$

Like in *Myhr et al.* [22] it is assumed that the inter-array cables are 33 kV 300 mm^2 copper core conduction cables, for which the costs per km are estimated to be 281 k€. Furthermore, it is assumed that the distance between two turbines is 1 km and the inter-array grid is divided into 20 strains, each connecting 5 turbines. To avoid damage of the cables the cable length between two turbines is set to 1.4 km plus the respective water depth.
Each of the strains of 5 turbines is then connected to the offshore substation. In [22] this results in a total inter-array cable length of 191.6 km for a water depth of 200m, of which 63.6 km of cable connect the 20 strains to the offshore substation. Thus, it was derived that the inter array cable length dependent on the water depth can be formulated as

$$L_{inter-array}(d) = 119.75 \cdot (1.4\text{km} + d) \tag{4.12}$$

The two options for the export cable are high voltage cables with alternating (AC) or direct (DC) current. AC cables suffer significant losses over a longer distance compared to DC cables. Therefore, it is assumed that DC cables are more likely to be used for a floating offshore wind farm. A detailed discussion of this can be found in [23]. For this thesis a single 320 kV 1500 mm^2 HVDC cable is used, as in [22], where the price of such a cable is estimated to be 443 k€/km. For simplicity it is assumed that the length of the export cable is the same as the distance to the closest shore, where the onshore substation is assumed to be.

For a floating offshore wind farm it is reasonable to assume that the offshore substation will also use a floating substructure. The costs for a 500 MW floating substation without installation are estimated with 161.7 M€ and the costs for its onshore counterpart with 71.5 M€ [22].

4.3.3 Costs for Installation and Commissioning

The costs for installation and commissioning include the costs for the assembly of the wind turbine on the substructure and transport to site, the installation of the

mooring system at the site, the installation of the electric cables and the installation of the offshore substation.

$$C_{I\&C}(d, L) = C_{iWT}(L) + C_{iMoorSys}(d, L) + C_{iCables}(L) + C_{iSubstation} \tag{4.13}$$

Bjerkseter and Ågotnes [23] discussed different installation procedures for FOWTs. Motivated by their most economical installation procedure it is assumed that the installation of the Windstar TLP system can be divided in six steps:

1. Floater and tower are preassembled on shore.
2. The structure is launched from the quay with a quayside lift. It is assumed that a single lift takes 2h.
3. Two tug boats transport the floater with tower to a crane barge near-shore.
4. The nacelle and preassembled rotor are lifted onto a barge, which tows the barge to the crane barge.
5. The nacelle and rotor are lifted by the crane barge with one lift each on the tower.
6. The complete system is towed by an AHTS, assisted with two tug boats, to the site and connected to the mooring system. The AHTS has a speed of $v_1 = 15$ knots by itself [22]. As the Windstar TLP system is stabilized with the outer columns and was designed to be towable [8] it is assumed that the AHTS has a speed of $v_2 = 5$ knots when towing the system, similiar to the WindFloat concept in [22]. A time consumption of 6 hours per mooring line is assumed for the attachment to the mooring system on site [22].

Since the installation procedure is dependent on the weather, different Operational weather Windows (OW) were considered. A detailed discussion for the OWs and how they affect the costs can be found in [23]. The calculation of the installation costs can be found in Appendix B.

This installation process can be divided in two parts: A fixed part, independent of the location, and a variable part that is dependent on the transportation time. For simplicity, it is assumed that the distance between the assembly site and wind farm site is the same as the closest distance to shore.

$$C_{iWT}(L) = C_{iWT1} + C_{iWT2}(L) \tag{4.14}$$

The constant part is about 412.5 k€, see appendix B. The second part can be calculated with

$$C_{iWT2}(L) = T_{transport} \cdot \frac{C_{AHTS}}{OW_{transport}} + 2T_{transport} \cdot \frac{C_{tugboats}}{OW_{transport}}, \tag{4.15}$$

where $T_{transport}$ is the transport time to site and return time of the vessels

$$T_{transport}(L) = \frac{L}{v_1} + \frac{L}{v_2}. \tag{4.16}$$

The daily rates for the AHTS C_{AHTS} and tug boats $C_{tugboats}$ can be found in table 4.2. The OW for the transport is assumed to be 54%, see reference [23].

Before the wind turbine can be installed, the mooring system has to be installed on site. The assumptions made for the installation costs of the mooring system are based on the assumptions made by *Bjerkseter and Ågotnes* [23]:

1. The installation of one gravity anchor takes 9 hours, due to their size.
2. The water depth influences the installation time by an additional 30 minutes per 100 m of water depth.
3. The anchors are installed with a single AHTS vessel. The vessel has 630 m^2 of storing capacity for the anchors. The capacity is assumed to decrease with one unit per 200 meter of increase in water depth, due to the storing capacity needed for the additional length of mooring lines. According to [52] the anchor has a height of 1.6 meters. With its volume of 833 m^2 it can be calculated that only a single anchor can be stored on one vessel.
4. The AHTS has a speed of 15 knots both with and without anchor on deck.
5. The operational windows for installation and transport are 60% and 75%, respectively.

With these assumptions the installation costs per mooring system can be calculated as follows

$$C_{iMoorSys}(d, L) = 3 \cdot \left(\frac{T_{iAnchor}(d)}{OW_{iAnchor}} + \frac{T_{tAnchor}(L)}{OW_{tAnchor}} \right) \cdot C_{AHTS} \tag{4.17}$$

The costs to install the export and inter-array cables are estimated to be 590 k€ and 190 k€, respectively. The installation cost for the floating offshore substation is set to approximately 18.5 M€ [22].

4.4 OPEX

The operational expenditures are the sum of the operation and maintenance costs and an insurance for the operating phase.

$$C_{OPEX}(L) = C_{O\&M}(L) + C_{InsO\&M} \tag{4.18}$$

4.4.1 Costs for Operation and Maintenance

The operation and maintenance costs per year in *Myhr et al.* [22] and *Bjerkseter and Ågotnes* [23] were calculated using an OMCE-calculator. The main assumption is that a mother vessel is operating within the wind farm at all times, with a shifting crew. The other assumptions and a detailed discussion of the made assumptions and maintenance strategies can be found in [23].
In this thesis, for simplicity, a linear function dependent on distance to shore was estimated based on their results, see figure 4.4:

$$C_{O\&M}(L) = (23 \frac{€}{km} \cdot L + 107300€) \cdot P_{WF}, \tag{4.19}$$

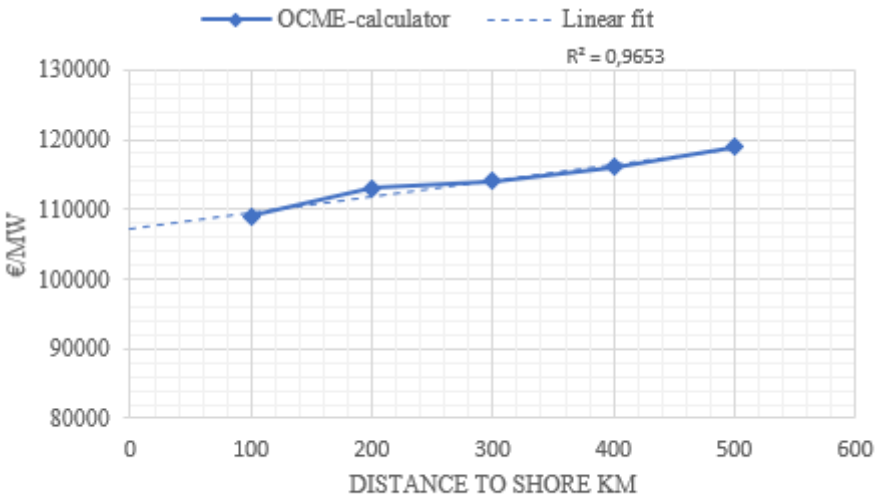

Figure 4.4: Estimated O&M costs depending on distance to shore. Results from OCME-calculator approximated from [23].

where P_{WF} ist the 500MW installed capacity of the wind farm. In addition to these costs an insurance for the operating phase is added which is estimated to be 17.5 k€/MW [22].

4.5 DECEX

4.5.1 Costs for Decommission

The decomission costs D_{Decex} can be estimated in relation to the installation costs. The assumed relations can be seen in table 4.3. The two options of either reusing the substructure or recycling and selling it as scrap are neglected in this work for the sake of simplicity.

Description	**% of installation cost**
Complete floating wind turbine	70
Subsea cables	10
Substation	90
Mooring systems	90

Table 4.3: Decommissioning cost in relation to installation cost [22].

4.6 LCOE

The LCOE can be calculated with the discounted CAPEX, OPEX and DECEX in relation to the generated energy. As mentioned earlier it is assumed that the development of the project takes 5 years and the wind farm operates for 20 years. The start of the development is in year 0 and the wind farm is build in year 4. Operation starts in year 5. The decomissioning takes place in year 26. Based on equation (2.15) the LCOE in the model is

$$LCOE = \frac{\sum_{t=0}^{n} \frac{C_{CAPEX}(d,L)+C_{OPEX}(d,L)+C_{DECEX}(d,L)}{(1+r)^t}}{\sum_{t=0}^{n} \frac{AEP}{(1+r)^t}}. \tag{4.20}$$

The CAPEX costs are distributed according to table 4.4 [23].

Year	**0**	**1**	**2**	**3**	**4**	**5**
Development and consenting	56%	10%	11%	11%	12%	1%
Construction phase insurance	-	25%	25%	25%	25%	-
Production costs (Turbine&Substructure)	-	-	19%	39%	42%	-
Mooring costs (incl. installation)	-	-	-	40%	60%	-
Grid costs (incl. installation)	-	20%	75%	5%	-	-
Installation of wind turbine	-	-	-	36%	64%	-

Table 4.4: Distribution of CAPEX costs from [23]

The annual O&M costs are distributed by 100% each year of operation until the wind farm is decomissioned. The DECEX costs are distributed by 100% in year 26. The used discount rate r in the model is 10%, as in the base case of reference [22].

5

Fatigue assessment in the time domain

During the lifetime of a FOWT it has to endure a series of short-term stresses caused by stationary environmental loads from wind and waves on the structure. These short-term stresses lead to short-term fatigue damages, which accumulate to long-term damages. As explained previously, the short-term fatigue damage can be estimated in the time and frequency domain. The time-domain approach first uses the rainflow-counting method and S-N-curve to calculate the damage per cycle of a stress time series and then the linear Palmgren-Miner rule to accumulate the final short-term damage of the time series. The procedure for the time-domain approach is visualized in figure 5.1.

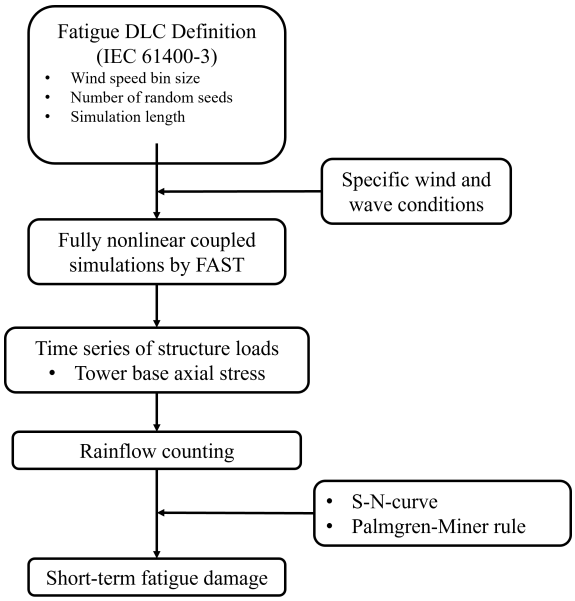

Figure 5.1: Procedure for short-term fatigue assessment in the time domain, adapted from [49]

FAST does not calculate the stress directly. Therefore, after performing six one hour simulations with different random seeds for each environmental condition the stress time series has to be calculated from the load time series. The most accurate way to calculate the stress would be to combine the FAST simulations with a finite element analysis and also consider stress concentration factors. However, for this

thesis a much simpler approach will be used and the stress will be derived using basic stress equations without considering stress concentration factors. As the tower base has to endure severe cyclic bending moments and axial forces due to nacelle and platform motions it will be the subject of study in this thesis. If the wind and wave directions are aligned it is convenient to only consider the axial stress at the lee side of the tower base using equation

$$\sigma_S = \frac{N_z}{A} + \frac{M_y}{W_y}. \tag{5.1}$$

This provides a conservative assessment. The axial force N_z and fore-aft bending moment M_y are output parameters of FAST. The nominal cross-sectional area of the tower base A and the area's sectional modulus W_y to the y-axis can be calculated with the inner- and outer diameters (D_i, D_o) of the tower base:

$$A = \frac{\pi}{4}(D_o^2 - D_i^2) \tag{5.2}$$

and

$$W_y = \pi \frac{(D_o^4 - D_i^4)}{32 D_o}, \tag{5.3}$$

respectively. A top view of the tower base cross section can be seen in figure 5.2

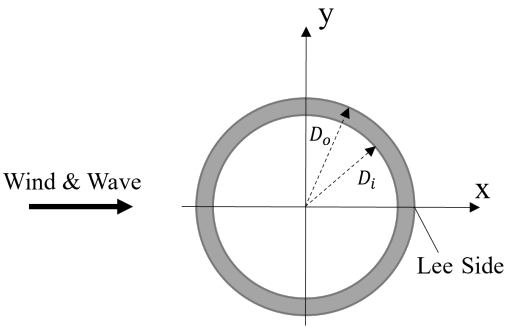

Figure 5.2: Top view of the tower base, adapted from [49]

When the time series of the stress is known rainflow cycle counting can be used to count the number of cycles per stress range. The rainflow cycle counting method used in this thesis is based on a mathematical definition by *Rychlik* [63]. Each local maximum of the stress time-series ν_i is paired with a particular local minimum u_i^{rfc}. The particular minimum for each maximum is determined with the following steps [64]:

1. Find the lowest values u_i^{back} and $u_i^{forward}$ between the time point of a local maximum ν_i and the nearest crossing point of the stress time-series with level ν_i, see figure 5.3.
2. The larger value of u_i^{back} and $u_i^{forward}$ is u_i^{rfc} and paired with the local maximum ν_i. For example in figure 5.3: $u_i^{rfc} = u_i^{forward}$ because $u_i^{forward} > u_i^{back}$.

The i-th rainflow pair (u_i^{rfc}, ν_i) has a stress range of $\Delta\sigma_s = \nu_i - u_i^{rfc}$.

If the next upcrossing of the level ν_i lies outside the time range it is an incomplete rainflow cycle. The maxima is then paired with u_i^{back} to form a cycle.

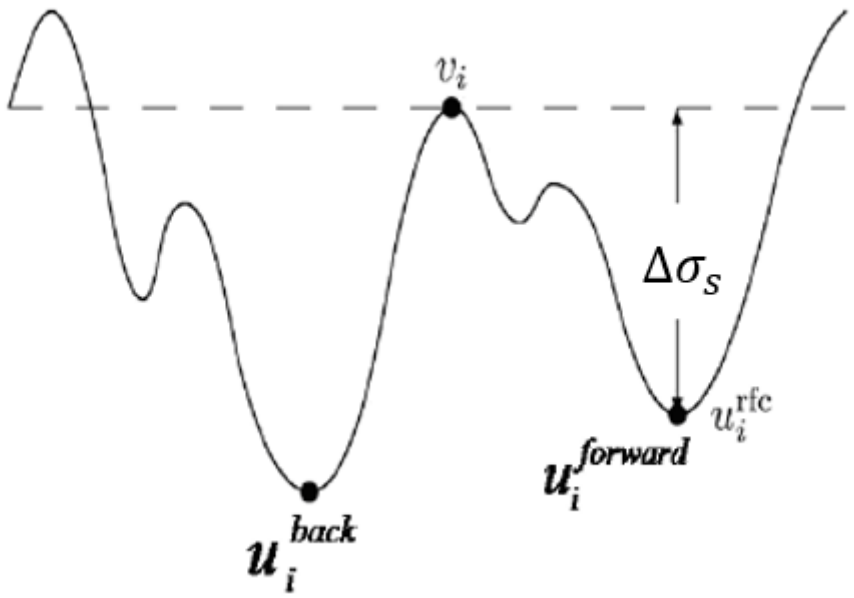

Figure 5.3: Rainflow counting method according to Rychlik, adapted from [64]

With the WAFO Toolbox in MatLab the turning points of the stress time series are identified and the stress cycles are counted with the previously explained algorithm. With the material parameters from the S-N-curve and the Palmgren-Miner-Rule the short-term damage occurring in the time-series can be calculated with equation (2.29). In this thesis a Wöhler exponent m of 3 and intercept parameter of $\log a = 12.436$ for the tower base are used. The values are taken from the DNV Classification Note No. 30.7 for steel base material in a corrosive environment [36]. The average damage occurring in the six simulations is used as the final damage per DLC.

6

Spectral fatigue approximation methods

With the help of the stress response spectrum $S_\sigma(\omega)$ the expected damage for Gaussian, narrow-banded loads can be estimated with the so-called narrow band approximation (NBA), which assumes that the stress ranges follow a Rayleigh distribution [38]:

$$D^{nb}(T) = \frac{1}{a} T f_z 2^{\frac{3m}{2}} \Gamma(1 + m/2) m_0^{m/2}, \tag{6.1}$$

where T is the time interval, f_z the zero-upcrossing frequency, $\Gamma(x)$ the gamma function and m and a the material parameters of the S-N-curve. The zeroth spectral moment m_0 and every other spectral moment can be calculated with equation (6.2):

$$m_n = \int_0^\infty \omega^n S_\sigma(\omega) d\omega. \tag{6.2}$$

The zero-upcrossing frequency is the number of zero-upcrossings of the stress in the considered time. In terms of spectral moments it can be estimated with

$$f_z = \frac{1}{2\pi} \sqrt{\frac{m_2}{m_0}}, . \tag{6.3}$$

As mentioned in chapter 2.6 the narrow band approximation can be corrected with correction factors for wide band properties and non-Gaussianity γ_{wb} and γ_{ng}, respectively, to improve the approximation of the expected damage [39]

$$D^{wb,ng}(T) = \gamma_{ng} \gamma_{wb} D^{nb}(T) = \gamma_{ng} D^{wb}(T). \tag{6.4}$$

The spectral fatigue approximation methods for broader spectra D^{wb} try to correct the narrow band approximation. They are based on the stress response's spectral moments. Some useful parameters for the calculation of the expected damage with wideband spectral approximations methods are listed below.

- The bandwidth parameters

$$\alpha_n = \frac{m_n}{\sqrt{m_0 m_{2n}}}. \tag{6.5}$$

  Note that $\alpha_n \leq 1$. The closer the bandwidth parameters are to one, the narrower the spectrum.

- The generalized average period T_n

$$T_n = 2\pi \left(\frac{m_0}{m_n}\right)^{1/n}. \tag{6.6}$$

- The average period between local maxima

$$T_m = 2\pi\sqrt{\frac{m_2}{m_4}}. \tag{6.7}$$

The already existing MatLab scripts to estimate the expected damage for different approximation methods are based on reference [46]. The following approximation methods are used in this work with the goal to obtain better results for more wide-banded spectra:

- *Benasciutti and Tovo* [42] proposed an approximation method which corrects the narrow band approximation with the bandwidth parameters α_1 and α_2. The method will be referred to as BenasTovo. The fatigue damage is

$$D^{BenasTovo} = (p + (1-p)\alpha_2^{m-1})D^{nb} \tag{6.8}$$

  where

$$p = (\alpha_1 - \alpha_2)\frac{1.112e^{2.11\alpha_2}(1 - \alpha_1 - \alpha_2 + \alpha_1\alpha_2) + (\alpha_1 - \alpha_2)}{(\alpha_2 - 1)^2} \tag{6.9}$$

- The approximation proposed by *Wirsching and Light* [43] will be referred to as WirschLight. It tries to correct the narrow band approximation with the help of the bandwidth parameter α_2. The fatigue damage is

$$D^{WirschLight} = \left(a(m) + (1 - a(m))\left(1 - \sqrt{1-\alpha_2}\right)^{b(m)}\right) D^{nb} \tag{6.10}$$

  with

$$a(m) = 0.926 - 0.033m \text{ and } b(m) = 1.587m - 2.323. \tag{6.11}$$

- The approximation proposed by *Lutes and Larsen* [65] will be referred to as LutLar. The method varies the generalized average period T_n, see equation (6.6), with the S-N-curve slope m. The fatigue damage is approximated with

$$D^{LutLar} = \frac{T}{a}\frac{m_0^{m/2}}{T_{2/m}} 2^{3m/2}\Gamma(1 + m/2) \tag{6.12}$$

- Steinberg's three band method [66] is based on the assumption that 68.3% of stress levels occur at two times the standard deviation, 27.1% at four times the standard deviation and 4.3% at six times the standard deviation of the stress signal. The method will be referred to as Steinberg. The fatigue damage is approximated with

$$D^{Steinberg} = \frac{T}{a}\left(\sqrt{\frac{m_2}{m_0}}\left(0.683(2\sqrt{m_0})^m + 0.271(4\sqrt{m_0})^m + 0.043(6\sqrt{m_0})^m\right)\right) \tag{6.13}$$

- The approximation proposed by *Chaudhury and Dover* [67] will be referred to as ChaDov. The fatigue damage is

$$D^{ChaDov} = \frac{T}{a}\frac{\Gamma(1+m/2)2^{3m/2}}{2\pi}m_0^{m/2}\sqrt{\frac{m_4}{m_0}} \times \left(0.5\alpha_2(1+F_a) + \left(\sqrt{(1-\alpha_2^2)}\right)^{m+2}\frac{\Gamma((1+m)/2)}{2\sqrt{\pi}\Gamma(1+m/2)}\right), \quad (6.14)$$

where

$$F_a = 0.3012\alpha_2 + 0.4916\alpha_2^2 + 0.9181\alpha_2^3 - 2.3534\alpha_2^4 - 3.3307\alpha_2^5 + 15.6524\alpha_2^6 - 10.7846\alpha_2^7. \quad (6.15)$$

- The approximation method by *Dirlik* [44] who proposed a mixture of an exponential and two Rayleigh distributions to approximate the Rainflow range distributions. This method will be referred to as the Dirlik method in the results section. The fatigue damage is

$$D^{Dirlik} = \frac{T}{a}\frac{m_0^{m/2}}{T_m}(D_1Q^m\Gamma(1+m) + (D_2|R|^m + D_3) \times \Gamma(1+m/2)2^{m/2}). \quad (6.16)$$

The parameters Q, R, D_1, D_2, D_3 are functions of the spectral moments. The functions can be found in [68].

- The approximation proposed by *Zhao and Baker* [45] used a similar approach as Dirlik. The method will be referred to as ZhaoBaker. The fatigue damage of the ZhaoBaker approximation is

$$D^{ZhaoBaker} = \frac{T}{a}\frac{(2\sqrt{m_0})^m}{T_m}((1-p)2^{m/2}\Gamma(1+m/2) + p(8-7\alpha_2)^{-m/\beta}\Gamma(1+m/\beta)), \quad (6.17)$$

where

$$\beta = \begin{cases} 1.1 & \alpha_2 <= 0.9 \\ 1.1 + 9(\alpha_2 - 0.9) & \alpha_2 > 0.9 \end{cases} \quad (6.18)$$

and

$$p = \frac{1-\alpha_2}{1-(8-7\alpha_2)^{-1/\beta}\Gamma(1+1/\beta)\sqrt{2/\pi}} \quad (6.19)$$

- The approximation proposed by *Sakai and Okamura* [40] will be referred to as SakOkam. The approximation cuts the stress response spectrum in two parts. For this thesis 1.6 rad/s was chosen as the cutting frequency. The periods $T_2(i)$ and zeroth spectral moment $m_0(i)$ with $i = 1, 2$ for the respective parts of the spectrum are used to calculate the fatigue damage

$$D^{SakOkam} = 2^{3m/2}\Gamma(1+m/2)\frac{T}{a}\left(\frac{m_0(1)^{m/2}}{T_2(1)} + \frac{m_0(2)^{m/2}}{T_2(2)}\right) \quad (6.20)$$

- The approximation proposed by *Jiao and Moan* [41] will be referred to as Jiao-Moan. Here the spectrum is also divided in two parts, splitting the spectrum in a fast and a slow component. The fatigue damage is

$$D^{JiaoMoan} = \left[\left(\left(\frac{m_0(1)}{m_0} \right)^{2+m/2} \left(1 - \frac{\sqrt{m_0(2)}}{\sqrt{m_0(1)}} \right) + \frac{m\Gamma((m+1)/2)\sqrt{\pi m_0(1) m_0(2)}}{m_0 \Gamma(1+m/2)} \right) \times \frac{c}{\sqrt{m_0 m_2}} + \left(\frac{m_0(2)}{m_0} \right)^{\frac{m-1}{2}} \frac{\sqrt{m_2(2)}}{\sqrt{m_2}} \right] D^{nb}, \tag{6.21}$$

where

$$c = \sqrt{m_0(1)m_2(1) + m_0(1)m_2(2) - \frac{m_0(1)}{m_0(2)}(m_1(2))^2} \tag{6.22}$$

6.1 Non-Gaussian correction methods

Since FAST performs non-linear simulations in the time domain it is likely that the resulting loads are also non-linear, or in other words non-Gaussian. In this thesis the correction factors proposed by *Winterstein* [48] and *Braccesi* [39] are used. The methods calculate a correction factor as a function of the Skewness and Kurtosis of the time series, or in case of the White-Noise approach of the Kurtosis estimation derived in 7.4.2. The Winterstein correction factor is calculated with the formula

$$\gamma_{ng}^{Winterstein} = \left(\frac{\sqrt{\pi} k}{2\Gamma(1+|\nu_2|)} \right)^m \left(\frac{\Gamma(1+m|\nu_2|}{\Gamma(1+\frac{m}{2})} \right). \tag{6.23}$$

The calculation of the variables k and ν can be found in Appendix C. Braccesi's proposed formula for a non-Gaussian correction factor is

$$\gamma_{ng}^{Braccesi} = e^{\frac{m^{3/2}}{\pi} \left(\frac{(Ku-3)}{5} - \frac{Sk^2}{4} \right)}. \tag{6.24}$$

For Gaussian-loads where the Skewness is zero and the Kurtosis equals three the correction factor equals 1. Typical values of the correction factor for non-Gaussian loads are slightly greater than 1.

7

Proposed spectral fatigue assessment approaches

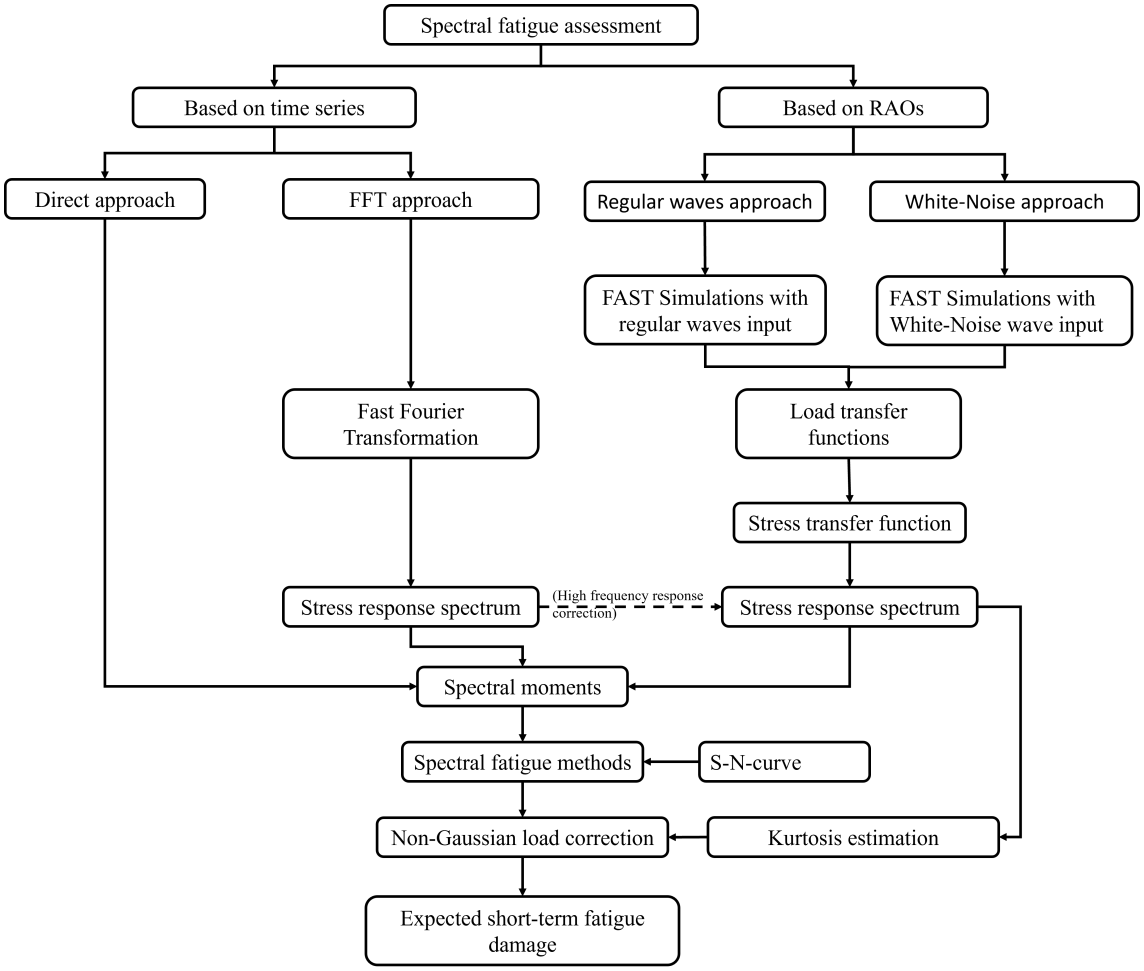

Figure 7.1: Flowchart of fatigue assessment in frequency domain

To be able to use the previously mentioned spectral approximation methods the spectral moments of the stress response spectrum have to be known. In this thesis four approaches on how to perform the spectral fatigue assessment with help of FAST simulations are proposed. The procedures are summarized in figure 7.1. They differ in the way the stress response spectrum and its spectral moments are determined. The two approaches on the left hand side of the figure are both based on the same stress time series as the fatigue assessment in the time domain. For the

two approaches on the right hand side new simulations are necessary, which aim at estimating the stress transfer function.

7.1 Direct approach

The direct approach calculates the spectral moments, necessary for approximating the expected fatigue damage, directly from properties of the stress time series. The motivation is to not add extra uncertainties by performing a fast-fourier-transformation to get the stress response spectrum. A disadvantage of this approach is that just the zeroth, second and fourth spectral moments can be calculated. The zeroth spectral moment is the same as the variance of the time series.

$$m_0 = var(\sigma_S(t)) \tag{7.1}$$

The second spectral moment can be calculated with help of the zero-upcrossing frequency. The zero-upcrossing frequency is the number of upcrossings per simulation time.

$$f_z = \frac{n_{up}}{T_{sim}}$$

To determine the number of upcrossings, the stress time series is shifted so that its mean value is equal to zero. In a next step the turning points are found with help of the WAFO Toolbox in MatLab. The number of upcrossings is increased by one if a negative turning point is followed by a positive turning point. After calculating the zero-upcrossings frequency and rearranging equation (6.3) the second spectral moment is

$$m_2 = (2\pi f_z)^2 m_0 \tag{7.2}$$

The fourth spectral moment can be calculated with the help of the average period between local maxima. The average period between local maxima for each simulation can be determined by first identifying the local maxima. If a turning point has a greater value than the preceding turning point it is regarded as a local maxima. Secondly, the time between the local maxima is averaged to get T_m. Then, by rearranging equation (6.7) the fourth spectral moment can be calculated with

$$m_4 = \left(\frac{2\pi}{T_m}\right)^2 m_2 \tag{7.3}$$

7.2 Fast-Fourier transformation approach

The FFT-approach is based on the same stress time series as the direct approach and the fatigue assessment in the time domain. A Fast-Fourier-Transformation is performed to get the one-sided power spectral density of the stress response for each DLC. Since there are six simulations per DLC a FFT is performed of each stress time series. The final stress response spectrum per DLC is the average one-sided power spectral density of the six simulations.

The spectral moments can be calculated with equation (6.2). This is done with the help of the WAFO Toolbox in MatLab. It is possible to calculate the zeroth, first, second, third and fourth spectral moments.

7.3 Regular waves approach

The goal of the regular wave and White-Noise approach is to determine the stress transfer function. This can be done with the help of simulations in FAST. In the regular wave approach, regular waves with a wave height of 2 m are used as input for FAST simulations without wind. It is assumed that the power spectral density of ocean waves is within a range of 0.2 rad/s to 2 rad/s. Therefore, just frequencies within this range are used for the regular waves. The simulation time per frequency is set to 1000 s but the first 200 s are cut off to mitigate transient effects. The resolution and accuracy of the RAOs depend on the frequency steps. For each step one simulation has to be performed. To achieve a high resolution, many simulations must therefore be carried out.

For each simulation with a regular wave frequency ω_i the load response is calculated with equation (2.22), where the amplitude of the input wave height is $X(\omega) = H/2 = 1\text{m}$. This leads to the following simplification

$$H(\omega_i) = Y(\omega_i), \tag{7.4}$$

where $Y(\omega_i)$ is the amplitude of the respective load output.

When the load transfer functions are known the stress transfer function is calculated with equation (2.25). Since the axial stress at the lee side of the tower base is of interest the stress RAO is

$$H_\sigma(\omega) = \frac{1}{A} \cdot H_{N_z}(\omega) + \frac{1}{W_y} \cdot H_{M_y}(\omega) \tag{7.5}$$

For each DLC in table 3.3 the stress response spectrum can then be calculated with equation (2.26), where the sea spectrum is dependent on the wave conditions of the DLC. The respective sea spectra were generated with help of the WAFO Toolbox, assuming a Pierson-Moskowitz sea spectrum.

7.4 White-Noise approach

Like for the regular wave approach, the goal for the White-Noise approach is to obtain the stress transfer function. In this approach a white-noise wave spectrum with a significant wave height is used as input for the FAST simulations. A perfect white-noise spectrum is characterized by having a constant energy density over the regarded frequency range. Therefore, a single simulation could be used to get the values of the load transfer functions over the entire regarded frequency range. However, as suggested in [34], six sets of simulations with different random seeds and a

length of 8000 s are carried out. The first 2000 s of the simulation time are cut off before post-processing.

To get the load transfer functions the power-spectral density of the wave elevation and cross-spectral density of the respective load and wave elevation are computed. The load transfer function is then calculated with equation (2.24).

The stress transfer function and stress response spectrum are obtained in the same way as in the regular wave approach. Followed by the calculation of the spectral moments with help of the WAFO Toolbox.

Both the White-Noise and regular wave approach estimate the stress response spectrum based on the stress transfer function. However, the White-Noise approach needs six simulations while the regular wave approach needs a simulation per frequency step. Therefore, the two approaches are compared below to determine if only one of the approaches should be used.

Furthermore, during the implementation of this approach it was observed that the approach has to be adapted if the effects of second order waves are considered, instead of only first order wave effects. These changes are also explained below.

First order wave effects only

The approach was initially tested only considering first-order wave effects. The range for the white-noise spectrum was set to 0 to 2 rad/s. The resulting stress transfer function for the tower base axial stress of the WindStar TLP system can be seen in figure 7.2, together with the stress RAO obtained from the regular wave approach. In both approaches the systems response to the pitch natural frequency at approximately 1.38 rad/s can be observed. The stress transfer function estimated with the White-Noise approach has a high resolution, while the RAO estimated with the regular wave approach only contains values at discrete frequency points. The values of both approaches at the discrete frequency points seem to be very close. Due to the similarity of obtained RAOs and the higher resolution at a much lower number of simulations, only the White-Noise approach will be considered moving forward.

The stress response spectra for the first and last DLC for first order wave effects only estimated with the RAOs obtained via the White-Noise approach can be seen in figures 7.3 and 7.4, respectively. The stress response spectra estimated with the RAOs obtained via the FFT-approach are also plotted for comparison. In the stress response spectra the peaks for the wave frequency response and pitch resonant response can be seen. At the pitch resonant response the response spectrum estimated with the White-Noise approach is slightly lower. However, it can be said that the response spectra estimated with both approaches are quite close.

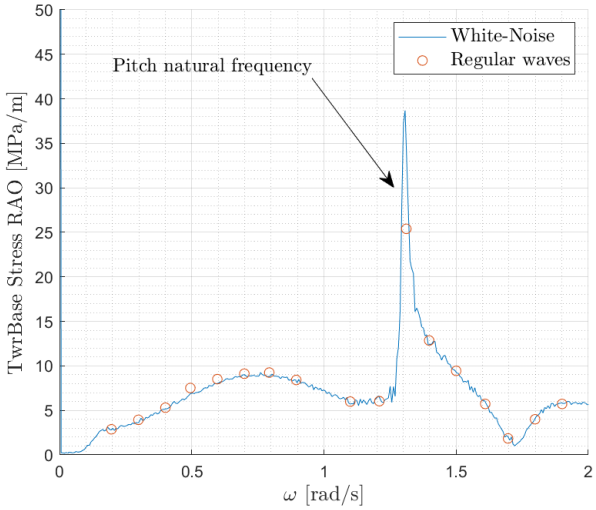

Figure 7.2: Comparison between RAOs estimated with regular wave input and white-noise input for first order waves forces only.

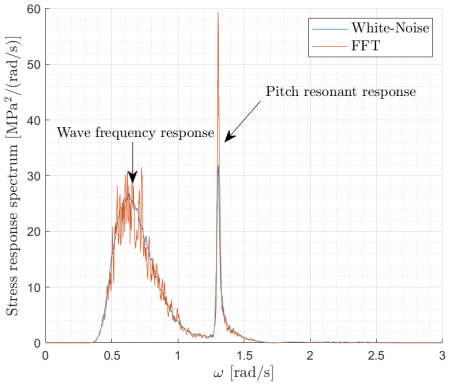

Figure 7.3: Stress response spectrum for first order waves only of sea state 1

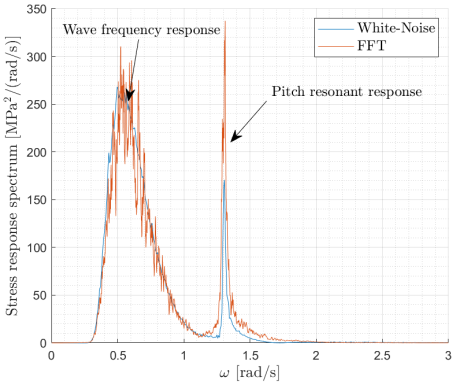

Figure 7.4: Stress response spectrum for first order waves only of sea state 15

First and second order wave effects

If second order wave effects are considered too the stress response spectrum has to be adapted to a frequency range of 0 to 1.6 rad/s. Otherwise it is not possible to capture the high frequency response for frequencies greater than 1.6 rad/s, which was observed for the WindStar TLP system by *Liu et al.* [49]. The resulting stress response spectra for the first and last DLC are shown in the figures 7.5 and 7.6, respectively. It can be seen clearly that the high frequency response is significantly overestimated with the White-Noise approach compared to the FFT-approach. To try to fix this overestimation a correction method is proposed in the following section 7.4.1.

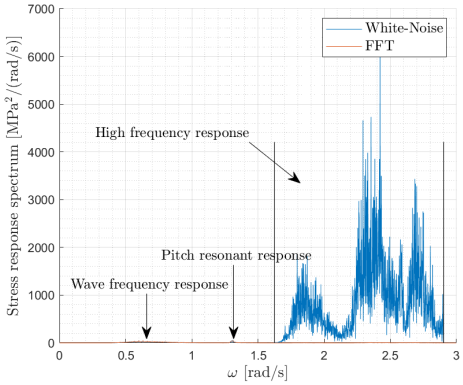

Figure 7.5: Stress response spectrum for first and second order wave effects of sea state 1

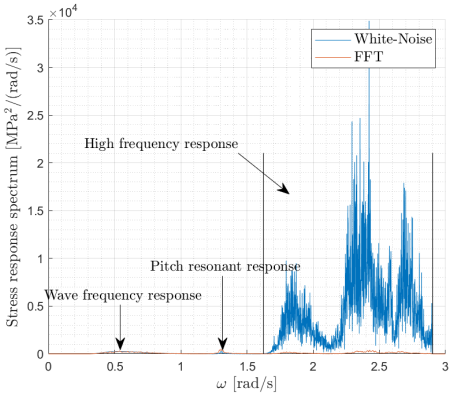

Figure 7.6: Stress response spectrum for first and second order wave effects of sea state 15

7.4.1 High frequency response correction

The stress response spectrum for each DLC derived via the FFT-approach can be regarded as correct. Therefore, it can be used as a reference to correct the stress response spectrum from the White-Noise approach. This is done by splitting both the spectrum estimated with the White-Noise approach and the spectrum estimated with the FFT-approach in three areas. The first area is from 0 to 1.6 rad/s. In this area the spectra from both approaches are very similar and no correction is necessary. The second area from 1.6 rad/s to 2.3 rad/s includes the first peak and the third area from 2.3 rad/s to 3 rad/s the second peak of the high frequency response. In these areas, the stress response spectrum estimated with the White-Noise approach significantly overestimates the stress response and therefore needs to be corrected. Since the first area before the peaks of the high frequency response remains unchanged, it is proposed to correct the high frequency stress response of the second and third area with a function dependent on the zeroth spectral moment of the first area. The proposed function for the corrected stress response spectrum $S_{\sigma,WN'}(\omega)$ has the form

$$S_{\sigma,WN'}(\omega) = a_i \cdot S_{\sigma,WN}^{b_i} \cdot m_{0,\omega<\omega_c}^{c_i}, \tag{7.6}$$

where in this case $\omega_c = 1.6$ rad/s.

The coefficients a_i, b_i and c_i are found by fitting the stress response spectrum of each DLC estimated with the White-Noise approach to the stress response spectrum estimated with the FFT-approach of the respective areas. For the second area in the frequency range from 1.6 to 2.3 rad/s the values for the coefficients a_2, b_2 and c_2 are estimated to be $a_2 = 0.0014$, $b_2 = 0.5$ and $c_2 = 1.5$, with a coefficient of determination (R^2) of 0.71.

The coefficients for the third area in the frequency range from 2.3 to 3 rad/s are estimated to be $a_3 = 0.0075$, $b_2 = 0.4$ and $c_2 = 1.4$, with a coefficient of determination (R^2) of 0.74.

The final corrected stress response spectrum is then denoted with

$$S_{\sigma,WN'}(\omega) = \begin{cases} S_{\sigma,WN} & 0 \leq \omega < 1.6 \\ 0.0014 \cdot S_{\sigma,WN}^{0.5} \cdot m_{0,\omega<1.6}^{1.5} & 1.6 \leq \omega < 2.3 \\ 0.0075 \cdot S_{\sigma,WN}^{0.4} \cdot m_{0,\omega<1.6}^{1.4} & 2.3 \leq \omega < 3 \end{cases} \tag{7.7}$$

The application of this correction method leads to the response spectra for the first and last DLC shown in the figures 7.7 and 7.8, respectively. Comparing the corrected stress response spectra with the previous stress response spectra in figures 7.5 and 7.6 it can be seen that the corrected spectra are much closer to the spectra obtained with the FFT approach.

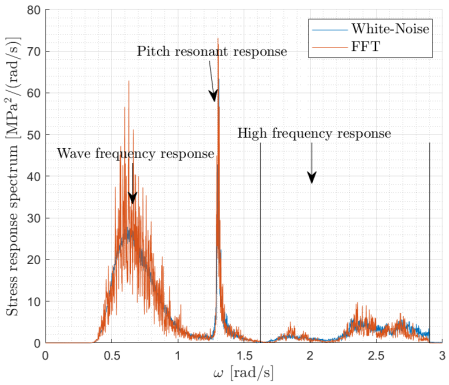

Figure 7.7: Corrected stress response spectrum for first and second order wave effects of sea state 1

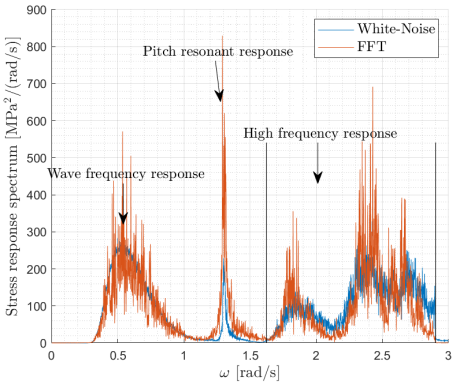

Figure 7.8: Corrected stress response spectrum for first and second order wave effects of sea state 15

7.4.2 Kurtosis estimation for nonlinear correction factors

Another problem of the White-Noise approach is that the Kurtosis and Skewness cannot be calculated based on the time series, due to lack of a time series. The Kurtosis and Skewness are necessary to calculate the Non-Gaussian correction factors of Winterstein or Braccesi. The problem is solved by first assuming that the Kurtosis is more important for the fatigue analysis and the Skewness is zero. The Kurtosis is then estimated as a function of the zeroth spectral moment

$$Ku = f(m_0) \tag{7.8}$$

Based on the Kurtosis of the time series and the zeroth spectral moment of the entire stress response of the FFT-approach, the following linear function was derived to estimate the Kurtosis in case only the first order wave effects are considered

$$Ku(m_0) \approx 0.0046 m_0 + 2.915. \tag{7.9}$$

If second order wave effects are also considered another function has to be used. This function was also derived from the Kurtosis of the time series but only the

zeroth spectral moment before the high frequency response starting at frequency ω_c is considered

$$m_0 = \int_0^{\omega_c} S_\sigma(\omega) d\omega. \tag{7.10}$$

The Kurtosis is then estimated with the linear function

$$Ku(m_0) \approx 0.0036 m_0 + 3.05, \tag{7.11}$$

where the coefficient of determination is 0.8.

The estimated Kurtosis together with the Kurtosis from the time series are plotted over the zeroth spectral moment in figure 7.9 if only first order wave effects. The same applies to figure 7.10 if second order wave effects are considered, too.

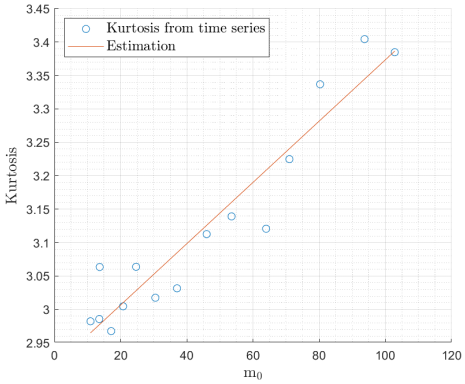

Figure 7.9: Estimation of Kurtosis based on zeroth spectral moment for first order wave effects only.

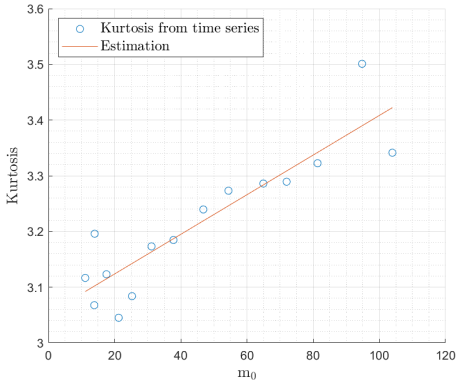

Figure 7.10: Estimation of Kurtosis based on zeroth spectral moment for first and second order wave effects.

8

Results LCOE-Model

8.1 Reference case

The first results for the LCOE model are for a reference case that uses the assumptions from the base case in *Myhr et al.* [22] for water depth, distance to the shore and annual energy production. The used boundary conditions are:

- The water depth at the wind farm site is 200 m.
- The distance to the closest coastline is 200 km.
- The capacity factor is set as 53%. With the losses mentioned in chapter 4 this results in a load factor of 44%. The annual energy production output of the 500 MW wind farm for this case is 1 930 262 MWh.

The capital expenditures per installed capacity for this case are summarized in table 8.1. The costs are divided into the three life phases of the project that contribute to the capital expenditures: Development and Consenting (D&C), Production and Acquisition (P&C), and Installation and Commission (I&C). The P&A costs for the mooring system include the mooring line and anchor costs. The electric grid costs include the costs to acquire electric cables and the offshore and onshore substations.

Life phase	**Description of costs**	**Costs for Reference Case**
D&C	Development and consenting	208,000.00 €
	Construction phase insurance	50,000.00 €
P&A	Turbine & Substructure	2,470,000.00 €
	Mooring System	123,000.00 €
	Electric Grid	751,000.00 €
I&C	Installation of wind turbine	138,000.00 €
	Installation of mooring system	82,000.00 €
	Installation of Electric Cables	309,000.00 €
	Installation of floating substation	37,000.00 €
CAPEX per MW		4,168,000.00 €/MW

Table 8.1: CAPEX per MW for Reference Case

The operational expenditures are summarized in table 8.2. The annual operation phase insurance costs are independent of the location. The annual operating and

maintenance costs were estimated for the reference case using equation (4.19).

Life phase	Description of Costs	Costs for Reference Case
O&M	Annual operating & maintenance costs	112,000.00 €
	Annual operation phase insurance costs	18,000.00 €
Annual OPEX per MW		130,000.00 €/(MW · year)

Table 8.2: Annual OPEX per MW for Reference Case

The costs occurring at the end of life during the decommissioning life phase are summarized in table 8.3. The costs are related to the installation costs in table 8.1 by the percentages summarized in table 4.3. Compared to the capital and annual operational expenditures the decommissioning expenditures are quite low.

Life phase	Description of Costs	Costs for Reference Case
DECOM	Decommissioning of wind turbine	97,000.00
	Decommissioning of electric cables	31,000.00
	Decommissioning of floating substation	33,000.00
	Decommissioning of mooring system	73,000.00
DECEX per MW		234,000.00

Table 8.3: DECEX per MW for Reference Case

By distributing the CAPEX, OPEX and DECEX costs according to the assumptions made in chapter 4.6 and putting the results in relation to the annual energy production the LCOE is estimated. The LCOE for the reference case is 177.8 €/MWh. The relative shares of CAPEX, OPEX and DECEX of the LCOE can be seen in figure 8.1. The capital expenditures were further split into different costs to get a better understanding of how the LCOE is comprised. It can clearly be seen that the major part of the LCOE with about 81 % is due to capital expenditures. The production costs for the wind turbine and substructure together with the grid costs, which include the acquisition and installation of the electric cables and the substations, are the main contributors to the capital expenditures.

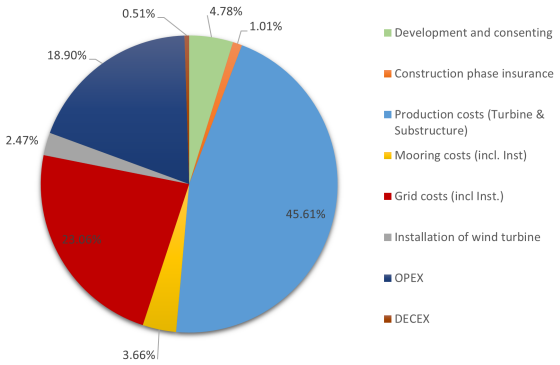

Figure 8.1: Composition of LCOE for reference case

8.1.1 Comparison to literature

The results for the reference case can be compared to the results of the WindFloat and Tension-Leg-Wind-Turbine (TLWT) concepts from *Myhr et al.* [22]. The semi-submersible WindFloat concept was chosen for comparison because it is closest in design to the WindStar TLP system. With a mass of 2500kg it is about 500 kg heavier than the WindStar TLP system.
The TLWT concept was chosen for comparison because it is a tension-leg platform like the WindStar TLP system. With just 417 tons it is much lighter than the WindStar TLP concept.

The CAPEX of the three different concepts can be seen in figure 8.2. Due to the different weights, the production costs for the WindStar concept are between the production costs of the WindFloat and TLWT concepts. The mooring costs for the TLWT are relatively high compared to the other two concepts due to a more complex mooring system. Overall, it can be concluded that the CAPEX results for the WindStar TLP system seem to be plausible compared to the results from *Myhr*.

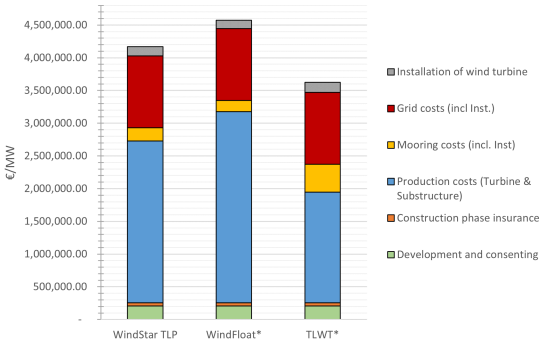

Figure 8.2: CAPEX comparison of WindStar TLP system to other concepts.*Windfloat and TLWT results from [22]

The LCOE and its composition for the three different concepts can be seen in figure 8.3. The Windfloat concept has a LCOE of about 190 €/MWh, the TLWT concept

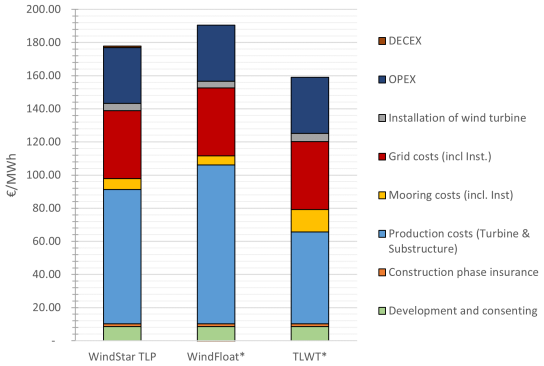

Figure 8.3: LCOE comparison of WindStar TLP system to other concepts.*Windfloat and TLWT results from [22]

160 €/MWh [22]. The minor differences in OPEX due to the symplification made in chapter 4.4 barely affect the LCOE. In *Myhr* it was assumed that the substructure is sold for scrap when decommissioned, which resulted in very low or even negative DECEX [22]. Due to the low contribution of DECEX to the LCOE, see figure 8.1, the different assumptions are barely affecting the LCOE.

8.2 LCOE-Model: North Sea

Instead of fixed assumptions for water depth, distance to the closest coastline and annual energy production, MetOcean and bathymetry data will now be used as input for the LCOE-model. The North Sea area from 50°N to 60°N latitude and 5°W to 12°E longitude is the area of interest. The longitudinal and latitudinal distance between two grid points is 0.1°.

The water depth and distance to the nearest coastline for this area can be seen in figures 8.4 and 8.5, respectively. The water depths range from 0 m to more than 3500 m in the North West part of the plot. Around Norways border the Norwegian trench can be seen. The southern part of the North Sea is relatively flat, often with water depths of less than 50 m.

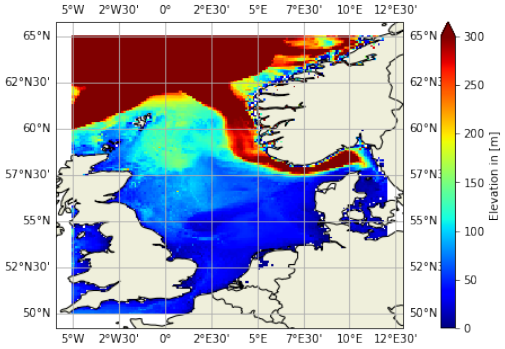

Figure 8.4: Water depth in the North Sea in meters

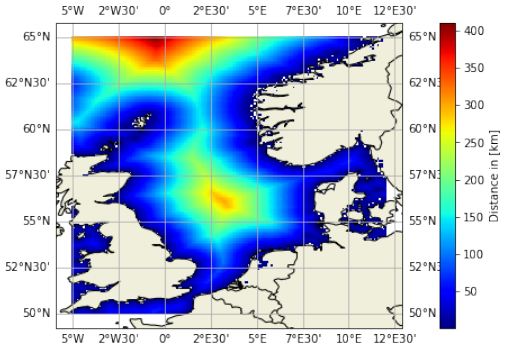

Figure 8.5: Distance to nearest coastline in kilometers for the North Sea area

The annual energy production can be estimated based on the wind data for every grid point according to chapter 4.2. The mean annual energy production for an installed capacity of 500 MW based on the years from 2016 to 2021 can be seen in figure 8.6. The figure shows the AEP after taking into account the losses assumed in chapter 4.6. The corresponding load factors can be seen in figure 8.7. It can clearly be seen that the AEP offshore is much higher than onshore. In general the AEP also increases with an increase of the distance to the coastline. The highest AEPs can be seen north of Scotland and south of Norway. The offshore load factors are significantly higher than the 44 % assumed in the previous section.

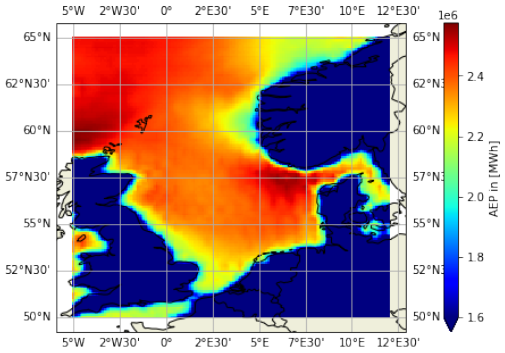

Figure 8.6: Mean annual energy production in the years 2016-2021.

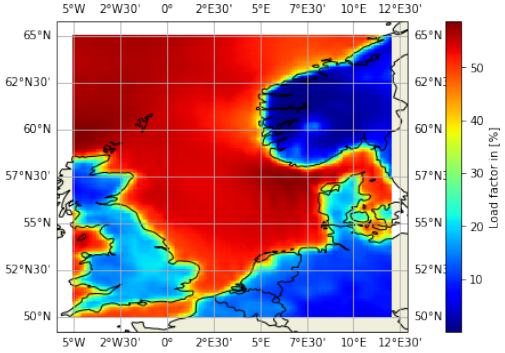

Figure 8.7: Load factors based on AEP.

The capital expenditures for the regarded area can be seen in figure 8.8. It ranges from about 3.5 M€/MW up to more than 5.5 M€/MW depending on where the wind farm is assumed to be located. The influence of distance to coast and water depth on the CAPEX is clearly visible. With an increase of distance, the CAPEX increases. At locations closer to the shore but with deep waters, like south of Norway, the costs increase, too. The highest costs are in the North West part of the map, where both water depth and distance to coast have their maxima.

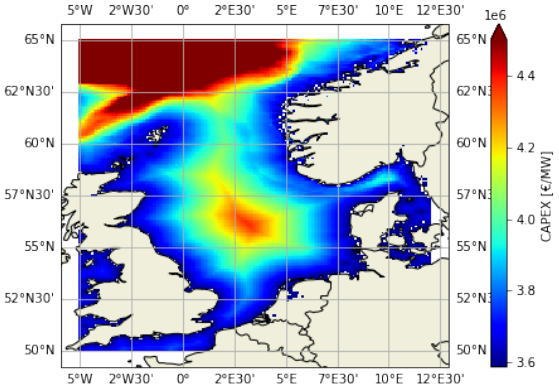

Figure 8.8: CAPEX per MW for North Sea area

The operational expenditures in the model are solely depending on the distance to coast. The annual OPEX can be seen in figure 8.9. They are linearly increasing with increasing distance. The costs range from 125 000 to 135 000 € per MW per year.

The decommissioning costs can be seen in figure 8.10. The DECEX costs are also mainly depending on the distance to coast due to their relation to the installation costs. The DECEX costs range from about 150 000 €/MW to 350 000 €/MW.

The resulting LCOE for each grid point in form of a map is shown in figure 8.11. It can be seen that the CAPEX and AEP mainly affect the LCOE. Close to the

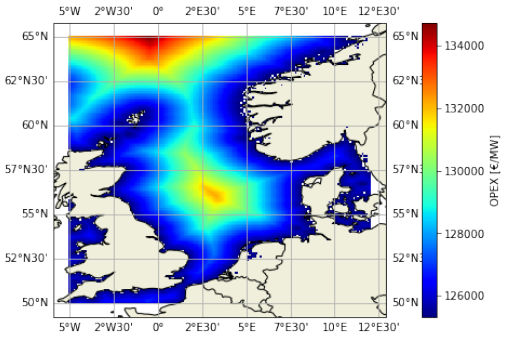

Figure 8.9: Annular OPEX per MW for North Sea area

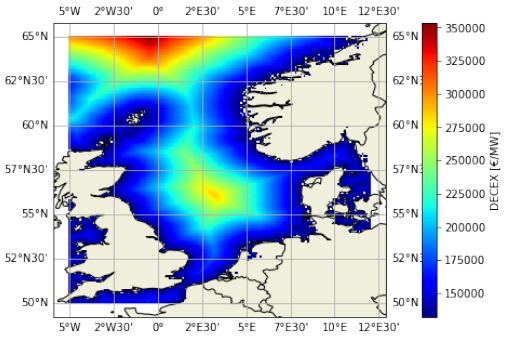

Figure 8.10: DECEX per MW for North Sea area

coastlines the LCOE is higher compared to further offshore due to a lower AEP. At the best locations the AEP is high but CAPEX relatively low. The best locations according to the model have LCOEs of about 122 €/MW. The highest LCOEs are around 180€/MW.

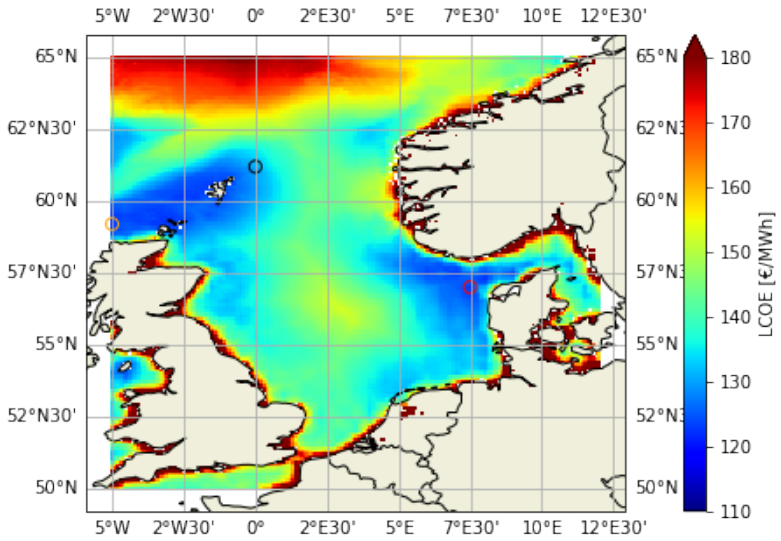

Figure 8.11: LCOE for the North Sea area

Two areas that seem to be favorable for floating offshore wind turbines in regard of LCOE are west of Denmark and north of Scotland. The red circle west of Denmark refers to the Location with the minimum LCOE (122€/MW) in the entire regarded North Sea area. It has to be noted that the water depth at this location is just 31 meters. It can be assumed that the use of a fixed foundation for the wind turbines instead of the floating substructure for water depths of up to 50 m would result in even lower electricity generation costs. If just locations with water depths of more than 50 meters are regarded the location marked with an orange circle north of Scotland has the lowest LCOE. The water depth at this location is 91 m, while it is one kilometer closer to the coastline than the first site. Due to the higher load factor, the LCOE is also 122 €/MWh. The third location is the location used for the fatigue assessment. The LCOE for this location is about 131 €/MWh.

	Site 1 (red circle)	**Site 2 (orange circle)**	**Site 3 (black circle)**
Distance to coast	49.00 km	48.00 km	59.00 km
Water depth	31.00 m	91.00 m	164.00 m
CAPEX	3,720,000.00 €/MW	3,740,000.00 €/MW	3,794,000.00 €/MW
Annual OPEX	126,420.00 €/MW	126,400.00 €/MW	126,660.00 €/MW
DECEX	156,700.00 €/MW	156,400.00 €/MW	162,400.00 €/MW
Load factor	57.80 %	58.10 %	54.90 %
LCOE	122.00 €/MWh	122.00 €/MWh	130.70 €/MWh

Table 8.4: Parameters of three different wind farm sites

Compared to the result in the reference case the LCOEs in table 8.4 are quite low. In addition to the change in costs, due to changes of water depth and distance to coast, the higher load factors play a major role in driving down the LCOE. This shows the importance of considering the actual wind resources at possible locations.

The cost model is only valid for the WindStar TLP system. So far, the WindStar TLP system is still at the concept stage, and apart from a miniature model for experimental testing, no real prototype has been built or installed. Therefore, knowledge of the actual production costs and installation process are limited. Furthermore, it is assumed that a floating substation and DC-export cable is used regardless of the water depth and distance to the coast. ERA5-reanalysis data is used to obtain the wind speed, the water depth is obtained from GEBCO bathymetry data and the distance to the nearest coastline from NASA's Ocean Biology Processing Group. Uncertainties within these datasets also add uncertainties to the cost model. For simplicity it was assumed that the length of the export cable and the distance to a port, for installation and maintenance purposes, is the same as the distance to the closest shore. Furthermore, assumptions for costs have been taken from literature without checking if they are still valid today, e.g the price for steel.
Due to these limitations, simplifications and assumptions made in the model, it has to be noted that the model is just an indicator for the LCOE. It could be used in a preliminary project stage to find good wind farm sites in regard to LCOE and compare them with each other. Another aspect that has to be considered when looking for possible offshore wind farm locations is restriction zones, e.g. military or shipping routes.

9

Case study: Fatigue Assessment

9.1 Reference Case: Rainflow-counting

The one hour short-term fatigue damages for every DLC approximated with help of the RFC-Method in the time-domain are used as reference results for the spectral fatigue methods. Figure 9.1 shows the short-term damage for every design load case for the following scenarios: First order wave effects only, first and second order wave effects and wind plus first and second order wave effects.
It can be seen that if only first order wave effects are considered it results in a very low damage compared to the other two scenarios. This could result in an optimistic design of the tower base. The highest fatigue damages result from the case of combined wind and waves. The additional damage compared to the same case without wind is mainly due to coupled effects of wind and waves. However, it is clearly visible that the main part of the fatigue damage can be contributed to the second order wave effects.
Therefore, it is especially important to accurately predict the damage resulting from the effects of first and second order waves.

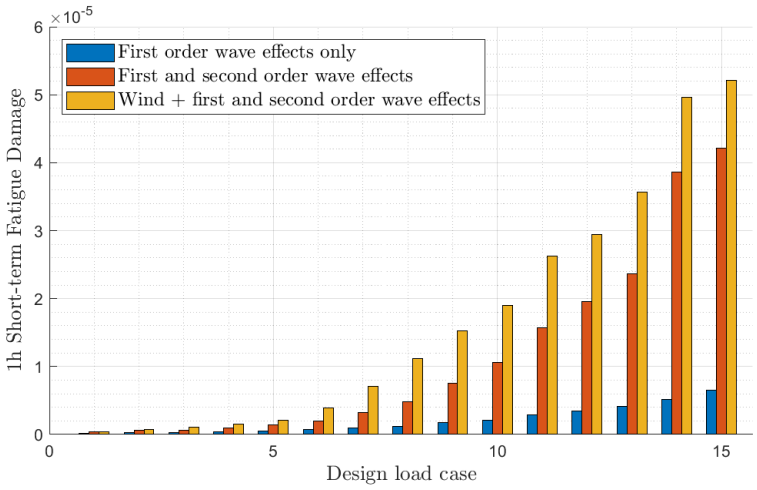

Figure 9.1: 1h short-term fatigue damage of DLCs for different scenarios calculated with RFC

9.2 Case 1: First order waves only

In this section the results of the proposed spectral fatigue assessment methods for first order wave effects only without wind are presented and compared to the RFC results. Based on the same time series as the RFC results, fatigue was estimated using the proposed direct approach without FFT and the FFT approach. Furthermore, the damage has been estimated using the stress transfer function derived from White-Noise simulations.

Direct approach

Based on the time series the zeroth, second and fourth spectral moments are calculated as proposed in chapter 7.1, without using a Fast Fourier transformation to obtain the stress response spectrum. The spectral moments are used with the NBA, ZhaoBaker and WirschLight approximations to estimate the expected one hour fatigue damage. Other spectral approximations cannot be used because they require other spectral moments that cannot be calculated directly. Additionally, the correction factors for Non-Gaussian loads by Winterstein and Braccesi are considered.
Table 9.1 shows the mean relative differences over each DLC to the RFC results for the different fatigue approximations, with and without Non-Gaussian correction. Comparing the different approximations without considering Non-Gaussian correction factors it can be seen that the NBA with 5% mean difference to the RFC results is much lower than the results for ZhaoBaker and WirschLight with about 27 % and 20%, respectively. Multiplying the NBA results with Winterstein's and Braccesi's correction factors further improves the difference to 3.8% and 1.8%, respectively.

Method	**Without correction**	**Winterstein**	**Braccesi**
NBA	5.00%	3.83%	1.76%
ZhaoBaker	26.61%	21.33%	23.50%
WirschLight	20.10%	14.43%	16.88%

Table 9.1: Mean relative difference of spectral approximation methods to RFC using the direct approach for first order wave effects only

The resulting expected fatigue damage of the different approximations for every DLC are shown in figure 9.2. It can be seen that every approximation follows the trend of the RFC fatigue damage. To get a better understanding of the stability of the different approximations the relative difference to the RFC results for each DLC can be seen in figure 9.3. The narrow band approximation without correction factor has good results for less severe sea states. For more severe sea states it underestimates the fatigue damage. If Winterstein's correction factor is used the fatigue is overestimated by close to 10% for less severe sea states, while the results for more severe sea states are closer to the RFC results. However, using Braccesi's correction factor the difference to the RFC results is always within 5%. Both the ZhaoBaker and WirschLight method underestimate the fatigue significantly for every DLC.

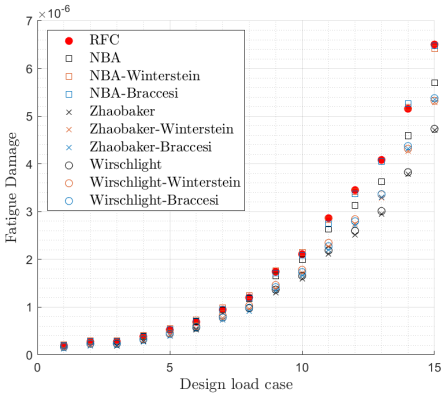

Figure 9.2: Fatigue damage from first order waves only for 15 DLCs. Calculated directly from the time series.

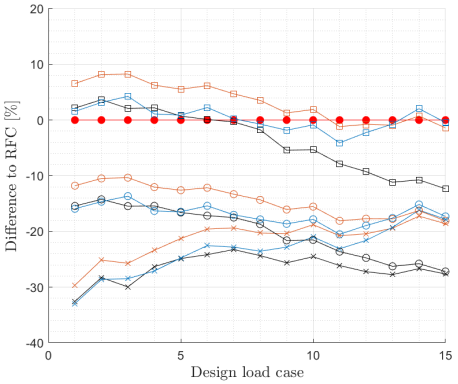

Figure 9.3: Relative difference of spectral approximation methods to RFC using the direct approach for first order wave effects only.

Fast-Fourier-Transformation approach

Now the stress response spectrum necessary for the estimation of the expected fatigue damage is obtained by performing a Fast Fourier Transformation of the stress time series and calculating the power spectral density. The mean difference to the RFC-results over every DLC can be seen in table 9.2. As can be expected based on the results of the direct approach, the mean differences to the RFC-results are the lowest for the NBA together with correction factors for Non-Gaussian loads. Furthermore, the results of the Dirlik, SakoKam and BenasTovo methods also have a relatively small difference to the RFC-results. These methods together with the NBA are further studied.

Method	Without correction	Winterstein	Braccesi
NBA	4.73%	4.04%	1.78%
Dirlik	3.92%	6.35%	3.33%
ZhaoBaker	13.63%	7.55%	10.21%
WirschLight	18.57%	12.82%	15.32%
SakoKam	5.41%	3.30%	2.04%
LutLar	11.46%	5.23%	7.96%
JiaoMoan	19.77%	28.29%	24.67%
Steinberg	5.65%	10.65%	7.49%
BenasTovo	11.75%	5.53%	8.24%
ChaDov	27.27%	22.19%	24.45%

Table 9.2: Mean relative difference of spectral approximation methods to RFC using the FFT-approach for first order wave effects only

Figure 9.4 shows the expected fatigue damage for the DLCs calculated with the FFT approach. As the importance of using a correction factor for Non-Gaussian loads can

already be concluded from table 9.2 and the direct approach, only methods with a correction factor are considered. The relative difference to the RFC-results for every DLC are shown in figure 9.5. It can be seen that the NBA and SakoKam method with Braccesi's correction factor are the most stable methods. Both are within 5% of the RFC-results for every sea state. Using Winterstein's correction factor results in an overestimation of fatigue for less severe sea states. Dirlik's method constantly overestimates the fatigue and the BenasTovo method constantly underestimates the fatigue, regardless of which Non-Gaussian correction factor is used. However, both methods are still within 10 % of the RFC-results for every DLC.

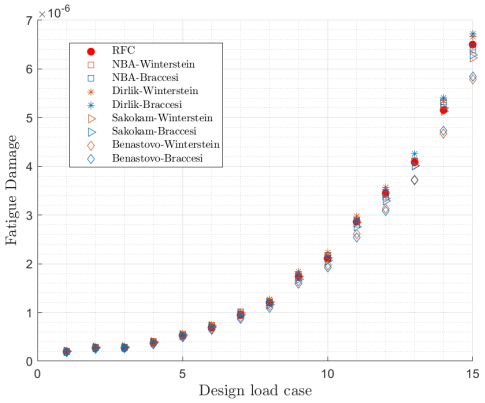

Figure 9.4: Fatigue damage from first order waves only for 15 sea states. Calculated with the FFT-approach.

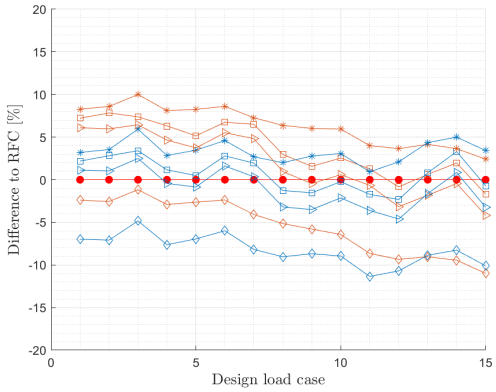

Figure 9.5: Relative difference of spectral approximation methods to RFC using the FFT-approach for first order wave effects only

White-Noise simulations

In this section the White-Noise approach for first order wave effects only without wind is used to estimate the expected damage. The mean relative difference to the RFC-results over every DLC for the different spectral approximations are shown in figure 9.3. The NBA method together with Braccesi's correction factor has a deviation of 3.62% from the RFC-results. With Winterstein's correction factor the mean relative difference is 4.97%.
Using the Dirlik approximation with Winterstein or Braccesi correction results in 7.32% and 4.3%, respectively. Furthermore, the Steinberg approximation with Braccesi correction results in a mean relative difference of about 5%. Using one of the other methods results in higher differences to the RFC-results.

Method	**Without correction**	**Winterstein**	**Braccesi**
NBA	7.12%	4.97%	3.62%
Dirlik	6.14%	7.32%	4.30%
ZhaoBaker	18.30%	12.56%	12.09%
WirschLight	21.91%	16.42%	18.83%
SakoKam	13.88%	7.84%	10.51%
LutLar	14.72%	8.73%	11.37%
JiaoMoan	16.29%	22.82%	19.23%
Steinberg	6.96%	8.13%	5.03%
BenasTovo	13.96%	7.90%	10.56%
ChaDov	34.16%	29.63%	31.74%

Table 9.3: Mean relative difference of spectral approximation methods to RFC using the White-Noise approach for first order wave effects only

Figure 9.6 shows the expected one hour fatigue damage for the NBA, Dirlik and Steinberg method with the different correction factors for Non-Gaussian loads. It can be seen that for the most severe sea states every method underestimates the fatigue damage. This is confirmed in figure 9.7, where the relative difference to the RFC-results for first order wave effects only is plotted. The NBA method with Braccesi's and Winterstein's correction factor both underestimate the damage by approximately 15 % for DLC 15. For the first ten DLCs the NBA with Braccesi's correction factor is in a range of 3 % to the RFC-result, while using Winterstein's correction factor results in an overestimation of up to 7%. The Dirlik approximation with Braccesi correction is always within a range of 10% of the RFC-results. The Steinberg approximation is close to the Dirlik approximation but overestimates the damage slightly more.

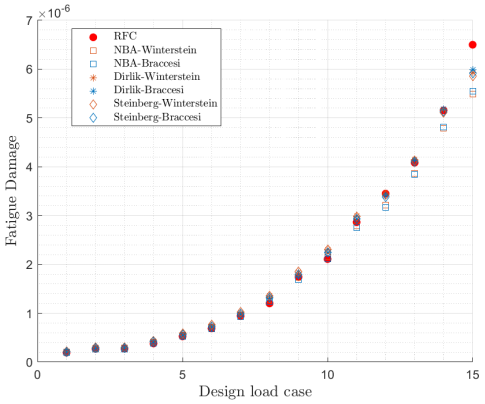

Figure 9.6: Fatigue damage from first order waves only for 15 DLCs. Calculated with the White-Noise approach.

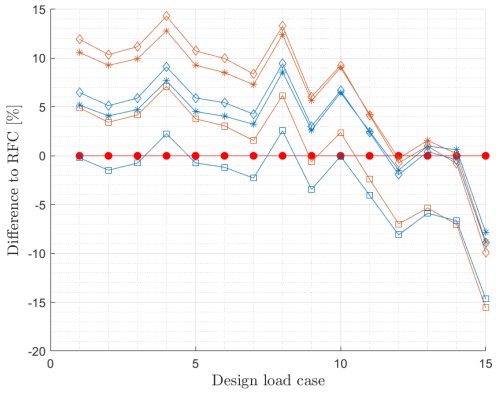

Figure 9.7: Relative difference of spectral methods to RFC using the White-Nose approach for first order wave effects only.

9.3 Case 2: First and second order waves

In this case the results of the proposed spectral fatigue assessment methods for first order and second order wave effects without wind are presented and compared to the RFC results. Based on the same time series as the RFC results, fatigue was estimated using the proposed direct approach without FFT and the FFT approach. Furthermore, the damage has been estimated using the stress transfer function derived with the White-Noise approach with a high-frequency response correction.

Direct from time series

Using the direct spectral approach based on the time series for combined first and second order wave effects results in the mean relative differences to the RFC-results over each DLC in table 9.4. The NBA approach without a Non-Gaussian load correction factor results in a mean relative difference of 8.52%. Applying Winterstein's or Braccesi's correction factor increases the difference to 18.34% and 16.29%, respectively. The ZhaoBaker method without a correction factor results in a mean difference to the RFC-results of 7.27%. If the correction factors are considered the difference decreases to 5.28% for Winterstein's and 6.31% for Braccesi's correction factor. With the WirschLight method, the differences are 9.4% without a correction factor. With Winterstein's and Braccesi's correction factors the mean difference is 1.81% and 3.58%, respectively

Figure 9.8 shows the one hour short-term damage for the different methods, with and without correction factors. Every method follows the trend of the RFC-results. For more severe sea states the NBA method clearly overestimates the damage. Looking at the relative differences to the RFC results for each DLC in Figure 9.9, it can be seen that the NBA method without correction factor constantly overestimates the fatigue by 5% to 10%. Applying a correction factor leads to an increase of the

Method	Without correction	Winterstein	Braccesi
NBA	8.52%	18.34%	16.29%
ZhaoBaker	7.27%	5.28%	6.31%
WirschLight	9.40%	1.81%	3.58%

Table 9.4: Mean relative difference of spectral approximation methods to RFC using the direct approach for first and second order wave effects

overestimation.
The ZhaoBaker method without a correction factor underestimates the fatigue damage by 18% for the first DLC and with about 5% for the last DLC. Applying the Non-Gaussian correction factors leads to a decrease of the underestimation for DLCs 1-6 with the Winterstein correction and 1-8 with the Braccesi correction. For the more severe sea states both correction methods result in an overestimation by up to 8%.
The WirschLight method without correction factors underestimates the fatigue by about 10% for every DLC. Applying the correction factors for Non-Gaussian loads decreases the underestimation. With the Winterstein correction the underestimation decreases to about 5% for the first DLC and further decreases with more severe sea states until DLC 9. For DLCs with sea states more severe the difference is within 0% and 2% of the RFC-results. With the Braccesi correction the underestimation for the first DLC is about 8%. Until DLC 11 the underestimation decreases. For more severe sea states the difference to the RFC-Results is within a range of 0% to 4%.

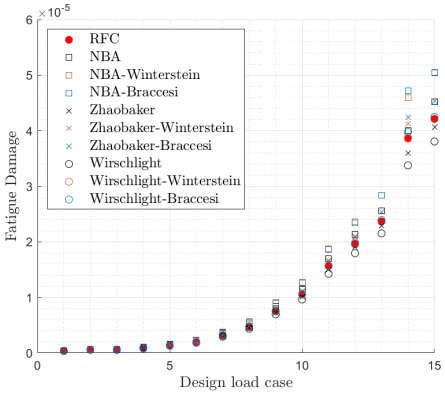

Figure 9.8: Fatigue damage from first and second order wave effects for 15 DLCs. Calculated directly from the time series.

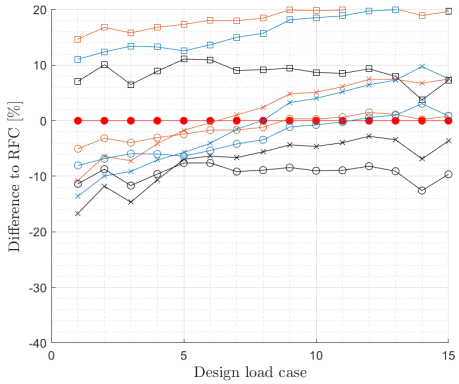

Figure 9.9: Relative difference of spectral approximation methods to RFC using the direct approach for first and second order wave effects.

Fast-Fourier-Transformation of time series

The mean relative differences over every DLC for every spectral method with and without correction factors can be seen in table 9.5. The most notable methods are the ZhaoBaker, WirschLight, Winterstein, BenasTovo and LutLar methods with correction factors for Non-Gaussian loads. Applying the ZhaoBaker method with the Winterstein or Braccesi correction results in a mean relative difference of 4.47% and 4.76%, respectively. With the WirschLight method the difference to the RFC-results is 1.42% with Wintersteins correction and 3.07% with Braccesis correction. The differences of the LutLar method are 2.76% and 4.81%, respectively. Using the BenasTovo method results in a mean relative difference to the RFC-results of 1.9% with the Winterstein and 3.65% with the Braccesi correction factor. The NBA method without a correction factor is 8.93%. With a correction factor for Non-Gaussian loads this difference increases to 18.78% and 16.72%, respectively.

Method	**Without correction**	**Winterstein**	**Braccesi**
NBA	8.93%	18.78%	16.72%
Dirlik	7.26%	10.16%	7.96%
ZhaoBaker	5.20%	4.47%	4.76%
WirschLight	8.88%	1.42%	3.07%
SakoKam	5.71%	8.01%	8.80%
LutLar	10.84%	2.76%	4.81%
JiaoMoan	34.87%	46.94%	44.28%
Steinberg	16.23%	26.75%	24.54%
BenasTovo	10.02%	1.90%	3.65%
ChaDov	51.36%	65.51%	62.99%

Table 9.5: Mean relative difference of spectral approximation methods to RFC using the FFT-approach for first and second order wave effects

Figure 9.8 shows the one hour short-term damages estimated with the above mentioned spectral methods with correction factors for the FFT approach together with the RFC-results. The overestimation of the NBA method is clearly visible, while the other spectral methods seem to better predict the fatigue damage. By looking at figure 9.11 a better understanding of the stability of the methods can be gained. The ZhaoBaker method with correction factors underestimates the damage for DLCs with less severe sea states and overestimates the damage for more severe sea states. The WirschLight method with Winterstein correction slightly underestimates the fatigue by about 3 % for the first DLC. For DLCs 6-15, the difference is within a range of -1% to 2%. With the Braccesi correction the underestimation for the first few DLCs is about 5%. For more severe sea states the underestimation decreases and for DLCs 10-15 the difference is within a range of -1% and 4 %. Like the WirschLight method, the LutLar method with correction factors also underestimate the fatigue damage for less severe sea states and are within a close range to the RFC-results for the more severe sea states.

Furthermore, the relative difference of the BenasTovo method with Braccesi correction to the RFC-results follows a similiar trend of underestimating the fatigue by a few percent for the first DLCs and converging towards 0% for more severe sea states. However, the BenasTovo method with Winterstein correction has a relative constant underestimation within a range of 1% to 3% of the RFC-results.

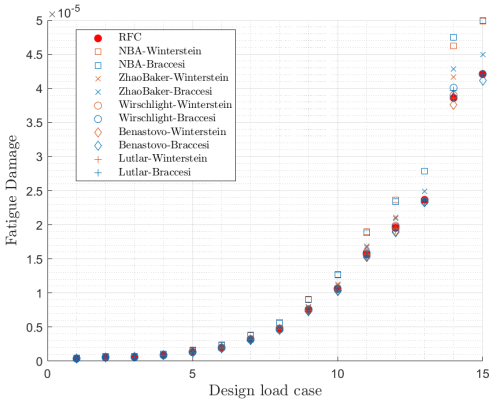

Figure 9.10: Fatigue damage from first and second wave effects for 15 DLCs.Calculated with the FFT-approach.

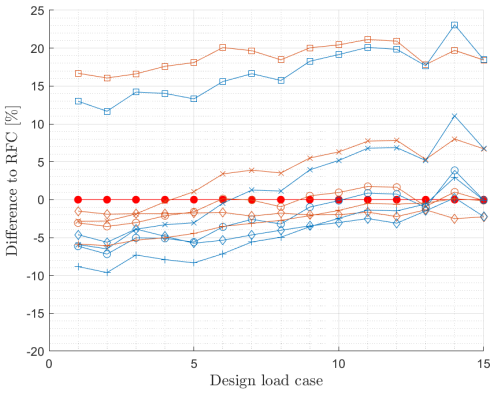

Figure 9.11: Relative difference of spectral approximation methods to RFC using the FFT-approach for first and second order wave effects.

White-Noise simulations

The mean relative differences of the various spectral approximations methods to the RFC results using the White-Noise approach if first and second order wave effects are taken into account are shown in table 9.6. All results include the high frequency response correction. The ZhaoBaker, WirschLight, LutLar and BenasTovo methods have the lowest mean differences to the RFC results. For the ZhaoBaker method the difference is about 5% with and without a correction factor. However, the difference is slightly lower than if a correction factor is used. For the other mentioned spectral methods the difference decreases if a correction factor for Non-Gaussian loads is applied. With the WirschLight method, the difference is 3.24% and 3.51% with the Winterstein and Braccesi corrections, respectively. The LutLar method results in mean differences to the RFC results of 4.41% and 4.85% with the respective correction factors. Applying the BenasTovo method with Winterstein's correction factor results in a mean relative difference of 3.63%. If Braccesi's correction factor is used the difference is 4.18 %. The NBA has a relatively high difference of 11.34% without a correction factor and 18.65% and 20.72% with the respective correction factors.

Method	**Without correction**	**Winterstein**	**Braccesi**
NBA	11.34%	20.72%	18.65%
Dirlik	8.57%	11.73%	9.72%
ZhaoBaker	4.64%	5.79%	5.21%
WirschLight	7.34%	3.24%	3.51%
SakoKam	3.95%	7.88%	7.35%
LutLar	10.21%	4.41%	4.85%
JiaoMoan	33.19%	44.91%	42.31%
Steinberg	18.27%	28.81%	26.60%
BenasTovo	9.25%	3.63%	4.18%
ChaDov	57.05%	71.44%	68.83%

Table 9.6: Mean relative difference of spectral approximation methods to RFC using the White-noise approach for first and second order wave effects.

The one hour short-term fatigue damages for the mentioned spectral methods with the White-Noise approach and correction factors for Non-Gaussian loads can be seen in figure 9.12. The relative differences for every DLC are plotted in figure 9.13. It can be seen that the NBA method with correction factors overestimate the fatigue damage by 8 to almost 30 %, depending on the DLC and used correction factor. The other spectral methods for more widebanded spectra are closer to the RFC-results. For the first three DLCs every wideband correction method slightly underestimates the fatigue damage. The biggest underestimation of up to 10% is by the LutLar method with Braccesi correction. The other methods underestimate the fatigue within a range of 0 to 8 %. For DLCs four to six all spectral methods except the LutLar method with Braccesi correction overestimate the damage: The ZhaoBaker method with Winterstein correction by almost 10%, the other methods by less. From DLC seven to twelve, each method is within a range of -6% to 6% of

the RFC results, with the WirschLight method being closest to 0%. All methods show an oscillation for the last three DLCs. DLC 13 is overestimated by up to 14% with the ZhaoBaker method, while DLC 14 is underestimated by up to 13% by the BenasTovo method. For the last DLC every method except ZhaoBaker is in a range of -1% to 4% of the RFC-results.

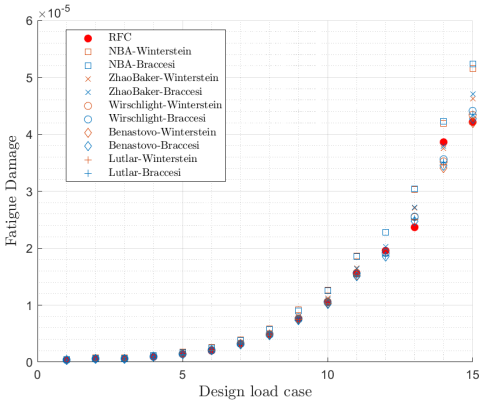

Figure 9.12: Fatigue damage from first and second order wave effects for 15 DLCs. Calculated with the White-Noise approach.

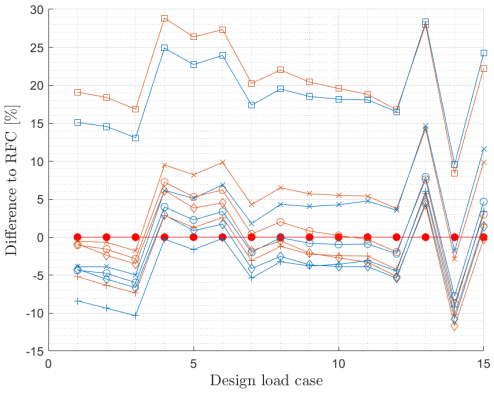

Figure 9.13: Relative difference of spectral approximation methods to RFC using the White-Noise approach for first and second order wave effects.

9.4 Case 3: Waves and wind

In this case the results of the proposed spectral fatigue assessment methods for wind combined with first and second order wave effects are presented and compared to the RFC results. Due to time limitations it was not possible to adapt the White-Noise approach to the combined wind and wave case. Therefore, only results of the direct and FFT approach can be shown in this section.

Direct from time series

Using the direct approach results in the mean relative differences summarized in table 9.7. The mean relative difference of the NBA is more than 50%. Using correction factors increases the difference further. The direct ZhaoBaker method has a mean difference to the RFC results of almost 75%, regardless of whether a correction factor is used or not. Using the direct WirschLight approach results in a difference 31% without a correction factor. With a correction method the differences are 39.89% and 35.69%, respectively.

Method	**Without correction**	**Winterstein**	**Braccesi**
NBA	58.60%	70.08%	64.95%
ZhaoBaker	77.03%	75.23%	75.85%
WirschLight	31.00%	39.89%	35.69%

Table 9.7: Mean relative difference of spectral approximation methods to RFC using the White-noise approach for combined wind and wave case.

The one hour short-term damage for each DLC is shown in figure 9.14. It can clearly be seen that the direct ZhaoBaker method underestimates the damage, while the NBA method overestimates it. The WirschLight method delivers the results closest to the RFC-results. A look at the relative differences between the individual DLCs in figure 9.15 can confirm this. For DLCs with more severe sea states the WirschLight results are within 20% of the RFC-results.

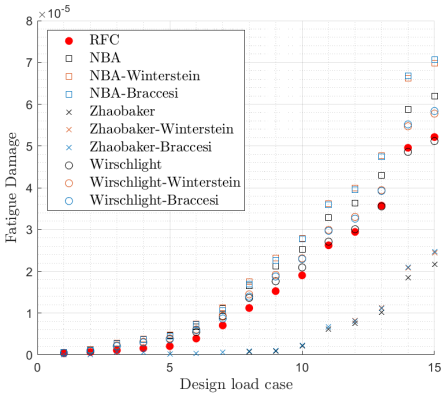

Figure 9.14: Fatigue damage from wind plus first and second order order wave effects for 15 DLCs. Calculated directly from the time series.

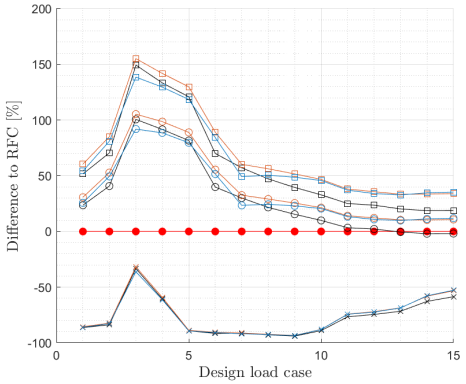

Figure 9.15: Relative difference of spectral approximation methods to RFC using the direct approach for combined wind and wave case.

Fast-Fourier-Transformation of time series

Table 9.8 summarizes the mean relative differences to the RFC results of the different spectral methods for the FFT approach. The difference of the NBA method without correction factors is 17%. Adding correction factors increases the difference to 25.44% and 21.98%, respectively. The lowest differences can be observed for the Dirlik, ZhaoBaker and WirschLight method with correction factors. For Dirlik the mean relative difference is close to 10%, regardless of which correction factor is used. The ZhaoBaker method with Winterstein correction results in a mean relative difference of 5.3%. Using the Braccesi correction leads to a difference of 6.22%. The WirschLight method results in a difference of 8.6% with Winterstein correction and 6.74% with Braccesi.

Method	**Without correction**	**Winterstein**	**Braccesi**
NBA	16.99%	25.44%	21.98%
Dirlik	13.50%	9.62%	9.57%
ZhaoBaker	10.52%	5.30%	6.22%
WirschLight	10.31%	8.60%	6.74%
SakoKam	17.69%	11.65%	13.49%
LutLar	32.13%	26.48%	28.16%
JiaoMoan	22.02%	31.56%	28.11%
Steinberg	24.38%	33.85%	30.15%
BenasTovo	25.10%	19.00%	20.97%
ChaDov	21.21%	30.73%	28.46%

Table 9.8: Mean relative differences of spectral approximation methods to RFC-results using the FFT-approach for combined wind and wave effects

The one hour short term damages for the above mentioned methods as well as

the results of RFC are shown in figure 9.14. The NBA overestimates and the Benas-Tovo method underestimates the fatigue damage. Looking at the relative differences to the RFC-results for every sea state in figure 9.17 it can be seen that the Dirlik, ZhaoBaker and WirschLight methods partly underestimate and partly overestimate the fatigue, dependent on the DLC. For DLCs with sea states more severe than DLC 6 the methods have a difference to the RFC-results in a range of 10%.

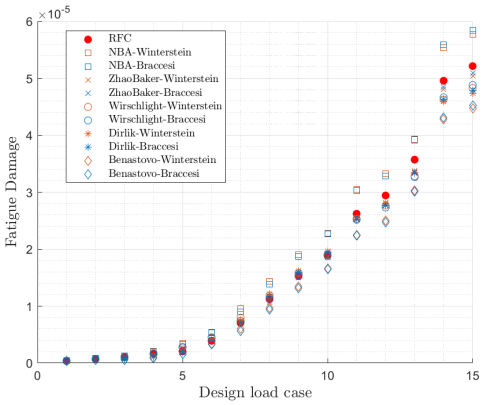

Figure 9.16: Fatigue damage from wind plus first and second order order wave effects for 15 DLCs. Calculated directly with the FFT-approach.

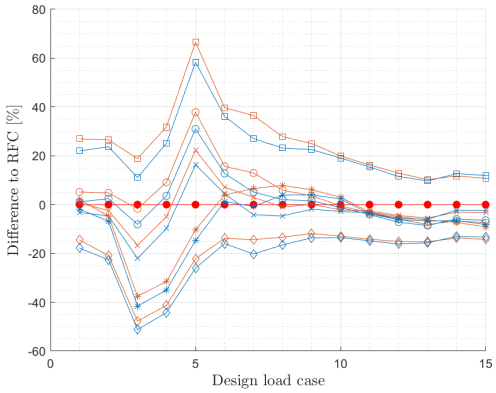

Figure 9.17: Relative difference of spectral approximation methods to RFC using the FFT-approach for combined wind and wave case.

9.5 Discussion

Limitations

When discussing the results, some limitations have to be kept in mind. The fatigue assessment has been performed assuming a turbine in operation. For example start-up, shut-down, emergency stops or extreme conditions have not been considered. The fatigue assessment is just performed for the tower base axial stress of the WindStar TLP system and a single location assuming a heading angle of zero degrees. The stress has been calculated with basic stress equations instead of performing a FEM analysis and taking a stress concentration factor into account. Furthermore, the effect of the mean stress level is not taken into account by e.g the Goodman correction. In case of the White-Noise approach for spectral fatigue assessment the wind effects are not considered, which leads to an underestimation of the fatigue damage.

Due to the aforementioned limitations and the objective of the paper, the focus of the discussion is not on a detailed fatigue assessment of the WindStar TLP system. The discussion rather focuses on the proposed approaches and spectral approximation methods for the estimation of the short-term damage in the frequency domain.

First order wave effects only

For the first case of first order wave effects only, the difference between the NBA method with and without Non-Gaussian correction factors with the direct and FFT approach are relatively low. This indicates that both approaches can be used. The same is true for the WirschLight method. However, the difference between the results of the ZhaoBaker method for the direct and FFT approaches is significant. Therefore, it can be concluded that the results from the FFT approach are more reliable. The FFT approach furthermore has the advantage that spectral methods depending on uneven spectral moments can be used.

For the direct and FFT approach, the NBA method with Braccesi's correction factor provides the results closest to the RFC-results compared to the other spectral approximation methods. For this reason, the NBA method should also be used for the White-Noise approach, although the Dirlik approximation with Braccesi correction is in the range of 10% of the RFC results for every DLC. This leads to two conclusions. First, if only first-order wave effects are considered, wideband correction is not necessary and the NBA gives good results. Secondly, it is necessary to use a non-Gaussian correction factor. In case of first order wave effects only, the Braccesi correction leads to more stable results over every DLC, which also leads to a lower mean relative difference to the RFC-results.

Figure 9.18 shows the one hour short-term damage estimated with the NBA method with Braccesi correction for the three different approaches. Using the NBA method with the direct and FFT-approach seems to be more reliable over every DLC than

with the White-Noise approach. This is because both are based on the original time series that was also used to estimate short-term damage in the time domain. Furthermore, the extra steps within the White-Noise approach, e.g estimating the Kurtosis based on the zeroth spectral moments, add extra uncertainties. Especially for the last DLC, the NBA method underestimates fatigue damage with the White-Noise approach. However, the White-Noise approach requires only 6 simulations to obtain the stress transfer function, which can be used together with a sea spectrum to estimate the expected fatigue damage for each possible combination of wave height and spectral peak period. In contrast, both the RFC and direct spectral and FFT approaches require 6 simulations per sea state to estimate the short-term damage. For a number of 15 sea states this results in a total number of 90 simulations.

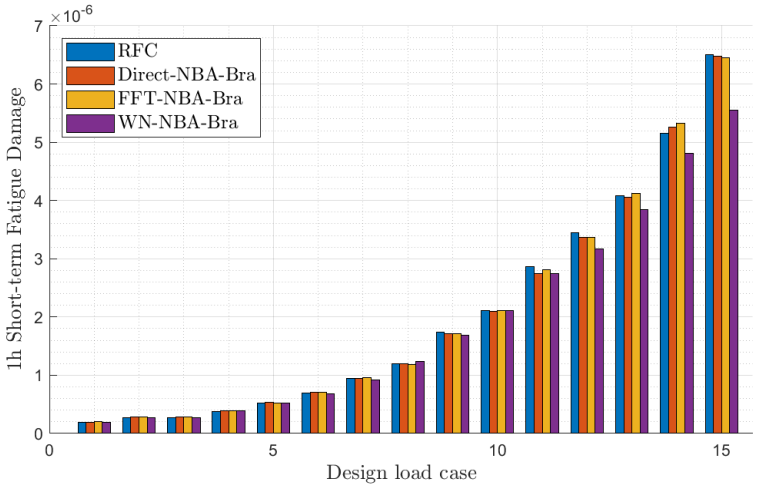

Figure 9.18: One hour short-term damage for different sea states for first order wave effects only.

First and second order wave effects

Comparing the direct and FFT approach for the second case, it can be said that the difference between the two approaches for the NBA and WirschLight method is small as in the first case. For this case, however, the results of the direct ZhaoBaker method of the two approaches are closer to each other. The results show that the NBA method constantly overestimates the fatigue damage, which can be expected for more widebanded response spectra. It can be concluded that a wideband correction method has to be used to estimate the fatigue more accurately.

Furthermore, it was concluded from the first case that it is necessary to use correction factors for a non-Gaussian load distribution to obtain better results. This can also be assumed if second order wave effects are additionally considered as this increases the non-linearity rather than decreasing it. The results of all three approaches for the second case confirm these assumptions since the differences with correction factor are smaller than without correction factor for the relevant spectral

approximation methods.

The results of the FFT approach for the second case show that the WirschLight and BenasTovo method with Winterstein correction are closest to the RFC-results. However, the BenasTovo method appears to be more stable with a relatively constant underestimation of only 1%-3%, while the WirschLight method varies somewhat more.

These two methods also show the best results with the White-Noise approach. However, the difference between the White-Noise results and the RFC results varies more than for the FFT-approach. This can be attributed to the fact that more steps, estimations and corrections for second-order wave effects have to be used for the White-Noise approach. In particular, the determination of RAOs, the correction of the high frequency response and the Kurtosis estimation lead to additional uncertainties in the results. Having said that, the results of the White-Noise approach with the WirschLight or BenasTovo method and Winterstein's correction factor are still within 10% of the RFC-results for every DLC. Keeping in mind the number of simulations necessary to compute the short-term damage this can be regarded as a very good estimation.

Since it was concluded that both the WirschLight and BenasTovo methods with the Winterstein correction give good results, the one-hour short-term damages estimated with the two spectral approximation methods for the different approaches are plotted in figure 9.19, if possible. Again, it can be seen that the results of all approaches, with exception of the White-Noise results for DLC 14, are close to the RFC results.

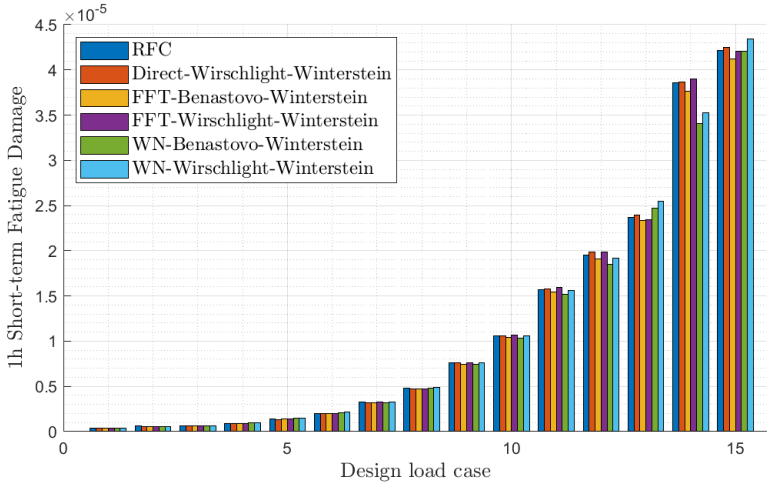

Figure 9.19: One hour short-term damage for 15 DLCs for first and second order wave effects.

Wind and waves

The results of the FFT and direct approaches for the third case are not as similar as for the other two cases. The comparison of the mean relative difference to the RFC results shows that the NBA method deviates by 40% more with the direct approach than with the FFT-approach. The WirschLight method on the other hand deviates by 20 % more with the direct approach compared to the FFT-approach. While using the ZhaoBaker method with the FFT-approach provides relatively good results, the results of the ZhaoBaker method with the direct approach are underestimating the fatigue significantly. Based on this observation and the differences between the ZhaoBaker method with the direct and FFT-approaches observed in the first case, it can be concluded that the FFT approach is more reliable than the direct approach. Therefore, if the spectral fatigue assessment is based on a time series, it is more likely that the FFT approach will give better and more reliable results than the direct approach.

Looking only at the results of the FFT approach, we can say that using the ZhaoBaker or WirschLight method with non-Gaussian correction factors provide the best results, as their mean relative differences to the RFC results are less than 10 %. However, for the combined wind and wave case it is not possible to say which non-Gaussian correction factor gives the better results. With the ZhaoBaker method, the Winterstein correction leads to a smaller mean relative difference than the Braccesi correction. With the WirschLight method it is exactly the opposite. The differences between the correction methods however are fairly low, with less than 1 % for the ZhaoBaker and less than 2% for the WirschLight method. This suggests that the choice of an appropriate wideband spectral method is more important than the choice of the non-Gaussian correction method.

Figure 9.20 shows the one hour short-term fatigue damages estimated with the methods regarded as giving the best results for the direct and FFT approach. In addition, figure 9.20 shows the RFC-results for comparison.

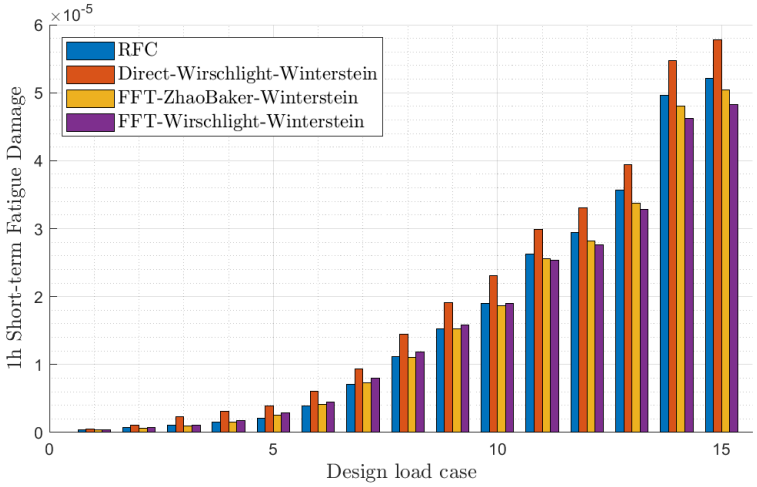

Figure 9.20: One hour short-term damage for 15 DLCs for the combined wind and wave case.

Within this thesis it was not possible to implement the White-Noise approach for the combined wind and wave case due to two main problems. First, the White-Noise approach is based on the stress RAO and a sea spectrum. The RAO puts the stress in relation with the wave height over the frequency spectrum. However, the stress occurring because of wind effects is not necessarily related to the wave height. Therefore, it is questionable if an accurate RAO can be found. Secondly, the main energy density of the wind is typically at low frequencies for which the energy density of the sea spectrum is close to zero. Since the stress response spectrum is estimated by multiplying the stress transfer function with the sea spectrum it would result in an underestimation of the wind effects.

10
Conclusion and outlook

In the first part of this thesis a LCOE-model for the WindStar TLP system was implemented. The model considers capital, operational and decommissioning expenditures. It is able to use MetOcean-Data to estimate the costs and annual energy production for different locations. The LCOE-model was compared to a similar model of other FOWT concepts in the literature. It was concluded that the results for the reference case are plausible. In a next step MetOcean-Data for the North Sea area was used as input for the LCOE-model. According to the results for the LCOE good locations for the WindStar TLP system are west of Denmark and north of Scotland. The results can be used as an indication of which locations are favorable for the WindStar TLP system as well as other FOWT concepts.

Many of the assumptions made for the estimation of costs in the LCOE model are based on another model from the year 2013. Therefore, they might be out-dated. In future work the LCOE-model could be improved by using more up-to-date assumptions, e.g for the steel price. Furthermore, a more detailed model of the operational expenditures should be implemented. The LCOE-model could also be extended by looking at restriction zones and excluding locations that are within the restriction zones and therefore unsuitable for wind farm sites.

Additionally, four approaches to estimate the short-term fatigue damage in the frequency domain based on FAST simulations were introduced in this thesis. The approaches were successfully implemented. After comparing the regular wave and White-Noise approach it was concluded that only the White-Noise approach will be studied further due to the number of simulations necessary to get a high resolution of the stress transfer function. It also became apparent that if second order wave effects are considered in the simulations, the stress response spectrum obtained with the White-Noise approach requires a high frequency response correction. For this purpose, a method was proposed that leads to stress response spectra that are closer to spectra obtained with the FFT-approach.
To obtain reference values the one hour short-term fatigue damage caused by the tower base axial stress was calculated via rainflow-counting and the Palmgren-Miner rule in the time domain for 15 DLCs. The three cases "first order wave effects only", "first and second order wave effects" as well as "wind combined with first and second order wave effects" were considered. For the same cases and 15 DLCs the expected one hour short-term fatigue damage was then estimated using the proposes approaches with different spectral approximation methods, with and without non-Gaussian correction factors. The results were compared to the RFC-results and

led to the following conclusions:

1. It is necessary to use a non-Gaussian correction factor regardless of the case. For the first case of first order wave effects only, the Braccesi correction factor provides the best results. For the second case, where first and second order wave effects are considered, the Winterstein correction factor provides the results closest to the RFC results. For the third case that additionally considers wind effects the differences between the non-Gaussian correction methods are negligible. It can be concluded that the choice of the spectral fatigue approximation method is more important than the choice of the Non-Gaussian correction method.
2. For the first order wave effects only case the NBA method produces results closest to the RFC-results.
3. For the more complex cases of second order wave effects or with wind, it is necessary to use a different spectral approximation method than the NBA method.
4. If first and second order wave effects are considered the Wirschlight or Benastovo approximations have the results closest to the RFC-results.
5. If wind is considered too, the Wirschlight and ZhaoBaker methods have the best results.
6. The FFT approach is more reliable than the direct and White-Noise approach. However, the same number of simulations is required as for the fatigue assessment in the time domain.
7. The White-Noise approach produces very good results with a limited number of simulations, if only first and first and second order wave effects are considered. The approach can so far just be used if the effects due to wind are neglected.
8. It is assumed that the White-Noise approach can be used to estimate the fatigue damage for every possible combination of wave height and peak spectral period, while the time domain approach and other spectral approaches need new simulations for other DLCs.

The fatigue assessment in this thesis was performed for a heading angle between wind and waves of 0 degrees. It would be interesting to investigate the spectral approach with different heading angles, as it is likely that much less simulations are necessary than in the time domain. Also, for a more exact approximation of the damage, the stress should be calculated with help of a finite element model of the system.
The most pressing issue of the White-Noise approach is that it does not take wind effects into consideration. Therefore, the approach should be extended in future works to take wind effects into account too. It might also be interesting to investigate how the small differences from the time-domain results for the spectral short-term damage estimates affect the lifetime damage. Furthermore, the White-Noise approach could be tested at other locations and for other FOWT concepts.

Overall, both the LCOE and spectral fatigue assessment methods presented in this

thesis can be used in an early planning and design stage of a project. The LCOE model can be used to identify the wind farm sites with the lowest LCOE. The proposed spectral fatigue assessment can then be applied to estimate the fatigue damage at these sites with relatively low computational effort, speeding up the design process. Nevertheless, in an advanced project phase, a site assessment based on wind and wave measurements and a conventional fatigue assessment in the time domain should be performed for certification purposes.

Bibliography

[1] DNV-GL. *Energy transition Outlook 2019*. DNV Report. 2019.

[2] M. D. Esteban et al. Why offshore wind energy? *Renewable energy* **36**.2 (2011), 444–450.

[3] DNV. *Floating offshore wind: The next five years*. DNV Report. 2022.

[4] L. Castro-Santos and V. Diaz-Casas. *Floating Offshore Wind Farms*. Cham: Springer International Publishing, 2016.

[5] D. Roddier et al. WindFloat: A floating foundation for offshore wind turbines. *Journal of renewable and sustainable energy* **2**.3 (2010), 033104.

[6] J. Jonkman. *Definition of the Floating System for Phase IV of OC3*. Tech. rep. National Renewable Energy Lab.(NREL), Golden, CO (United States), 2010.

[7] J. Koh et al. *Validation of a FAST Model of the SWAY Prototype Floating Wind Turbine*. Tech. rep. National Renewable Energy Lab.(NREL), Golden, CO (United States), 2016.

[8] Y. Zhao, J. Yang, and Y. He. Preliminary Design of a Multi-Column TLP Foundation for a 5-MW Offshore Wind Turbine. *Energies* **5**.10 (2012), 3874–3891.

[9] R. Gasch. *Windkraftanlagen: Grundlagen, Entwurf, Planung und Betrieb*. 4., vollständig überarbeitete und erweiterte Auflage 2005. Springer eBook Collection Computer Science and Engineering. Wiesbaden: Vieweg+Teubner Verlag, 2005.

[10] M. C. Brower. *Wind resource assessment: A practical guide to developing a wind project*. Online-Ausg. Hoboken, N.J: Wiley, 2012.

[11] T. von Karman. Progress in the statistical theory of turbulence. *Proceedings of the National Academy of Sciences of the United States of America* **34**.11 (1948), 530.

[12] J. C. Kaimal et al. Spectral characteristics of surface-layer turbulence. *Quarterly Journal of the Royal Meteorological Society* **98**.417 (1972), 563–589.

[13] J. Mann. The spatial structure of neutral atmospheric surface-layer turbulence. *Journal of fluid mechanics* **273** (1994), 141–168.

[14] B. Le Méhauté. *An introduction to hydrodynamics and water waves*. Springer Science & Business Media, 2013.

[15] L. H. Holthuijsen. *Waves in oceanic and coastal waters*. Cambridge university press, 2010.

[16] S. Chakrabarti. *Handbook of offshore engineering*. Vol. 2. Elsevier Science & Technology, 2005.

[17] O. Faltinsen. *Sea loads on ships and offshore structures*. Vol. 1. Cambridge university press, 1993.

[18] W. J. Pierson Jr and L. Moskowitz. A proposed spectral form for fully developed wind seas based on the similarity theory of SA Kitaigorodskii. *Journal of geophysical research* **69**.24 (1964), 5181–5190.
[19] K. Hasselmann et al. Measurements of wind-wave growth and swell decay during the Joint North Sea Wave Project (JONSWAP). *Ergaenzungsheft zur Deutschen Hydrographischen Zeitschrift, Reihe A* (1973).
[20] International Renewable Energy Agency. Renewable Energy Cost Analysis: Wind Power (2012).
[21] A. Ioannou, A. Angus, and F. Brennan. A lifecycle techno-economic model of offshore wind energy for different entry and exit instances. *Applied Energy* **221** (2018), 406–424.
[22] A. Myhr et al. Levelised cost of energy for offshore floating wind turbines in a life cycle perspective. *Renewable Energy* **66** (2014), 714–728.
[23] C. Bjerkseter and A. Agotnes. "Levelised Costs of Energy for Offshore Floating Wind Turbine Concepts". Master's Thesis. Norwegian Universitty of Life Sciences, 2013.
[24] J. M. Jonkman, M. L. Buhl, et al. *FAST user's guide*. Vol. 365. National Renewable Energy Laboratory Golden, CO, USA, 2005.
[25] J. M. Jonkman. *Dynamics modeling and loads analysis of an offshore floating wind turbine*. University of Colorado at Boulder, 2007.
[26] T. T. Tran and D.-H. Kim. A CFD study into the influence of unsteady aerodynamic interference on wind turbine surge motion. *Renewable Energy* **90** (2016), 204–228.
[27] P. J. Moriarty and A. C. Hansen. *AeroDyn theory manual*. Tech. rep. National Renewable Energy Lab., Golden, CO (US), 2005.
[28] Y.-s. Zhao et al. Time Domain Response Analysis of a Multi-column Tension-leg-type Floating Wind Turbine. *The International Society of Offshore and Ocean Engineers* (2014).
[29] K. F. Müller. "Probabilistic Fatigue Load Assessment for Floating Wind Turbines". PhD Thesis. Stuttgart: University of Stuttgart, 2019.
[30] J. M. Jonkman, A. Robertson, and G. J. Hayman. HydroDyn user's guide and theory manual. *National Renewable Energy Laboratory* (2014).
[31] Y.-s. Zhao et al. Coupled dynamic response analysis of a multi-column tension-leg-type floating wind turbine. *China Ocean Engineering* **30**.4 (2016), 505–520.
[32] Y. Bae. Development of a dynamic mooring module feam for fast v8. *Texas A&M University (TAMU), TX, USA* (2014).
[33] H. Wu et al. Transient response of a TLP-type floating offshore wind turbine under tendon failure conditions. *Ocean Engineering* **220** (2021), 108486.
[34] G. Ramachandran et al. "Investigation of response amplitude operators for floating offshore wind turbines". *The Twenty-third International Offshore and Polar Engineering Conference*. OnePetro. 2013.
[35] P. Stoica, R. L. Moses, et al. Spectral analysis of signals (2005).
[36] DNV CN 30.7. *Fatigue Assessment of Ship Structures*. DNV Classification Note No. 30.7. 2014.
[37] DNVGL-RP-C203. *Fatigue design of offshore steel structures*. Recommended Practice. 2016.

[38] I. Rychlik. On the 'narrow-band'approximation for expected fatigue damage. *Probabilistic Engineering Mechanics* **8**.1 (1993), 1–4.

[39] C. Braccesi et al. The frequency domain approach in virtual fatigue estimation of non-linear systems: The problem of non-Gaussian states of stress. *International Journal of Fatigue* **31**.4 (2009), 766–775.

[40] S. Sakai and H. Okamura. On the distribution of rainflow range for Gaussian random processes with bimodal PSD. *JSME international journal. Ser. A, Mechanics and material engineering* **38**.4 (1995), 440–445.

[41] G. Jiao and T. Moan. Probabilistic analysis of fatigue due to Gaussian load processes. *Probabilistic Engineering Mechanics* **5**.2 (1990), 76–83.

[42] D. Benasciutti and R. Tovo. On fatigue damage assessment in bimodal random processes. *International journal of fatigue* **29**.2 (2007), 232–244.

[43] P. H. Wirsching and M. C. Light. Fatigue under wide band random stresses. *Journal of the Structural Division* **106**.7 (1980), 1593–1607.

[44] T. Dirlik. "Application of computer in fatigue analysis". Ph.D. thesis. School of Engineering, UK: Univ. of Warwick, 1985.

[45] W. Zhao and M. J. Baker. On the probability density function of rainflow stress range for stationary Gaussian processes. *International Journal of Fatigue* **14**.2 (1992), 121–135.

[46] A. Bengtsson and I. Rychlik. Uncertainty in fatigue life prediction of structures subject to Gaussian loads. *Probabilistic Engineering Mechanics* **24**.2 (2009), 224–235.

[47] A. Adilah, K. Iijima, and T. Inoue. Spectral Approach for Fatigue Damage Evaluation of Floating Offshore Wind Turbine under Combined Wind and Wave Loads by Considering the Coupling Effect (2020).

[48] S. R. Winterstein. Nonlinear vibration models for extremes and fatigue. *Journal of Engineering Mechanics* **114**.10 (1988), 1772–1790.

[49] J.-R. Liu et al. "Effects of Second-order Wave Force on Fatigue Damage Assessment of a TLP-type Floating Wind Turbine". *The 30th International Ocean and Polar Engineering Conference*. OnePetro. 2020.

[50] J. Jonkman et al. *Definition of a 5-MW reference wind turbine for offshore system development*. Tech. rep. National Renewable Energy Lab.(NREL), Golden, CO (United States), 2009.

[51] Y. Zhao, J. Yang, and Y. He. "Concept Design of a Multi-Column TLP for a 5MW Offshore Wind Turbine". *Volume 7: Ocean Space Utilization; Ocean Renewable Energy*. American Society of Mechanical Engineers, 2012, pp. 225–232.

[52] Y.-s. Zhao et al. Experimental Study on New Multi-Column Tension-Leg-Type Floating Wind Turbine. *China Ocean Engineering* **32**.2 (2018), 123–131.

[53] S.-H. Xie et al. "Prediction of Springing-induced Extreme Responses of a TLP-Type Floating Wind Turbine". *The 30th International Ocean and Polar Engineering Conference*. OnePetro. 2020.

[54] IEC. *61400-3, Wind Turbines-Part 3: Design Requirements for Offshore Wind Turbines*. IEC Standard. 2009.

[55] DNVGL-ST-0119. *Floating wind turbine structures*. DNV Standard. 2018.

[56] L. Haid et al. “Simulation-length requirements in the loads analysis of offshore floating wind turbines”. *International Conference on Offshore Mechanics and Arctic Engineering*. Vol. 55423. American Society of Mechanical Engineers. 2013, V008T09A091.
[57] GEBCO Compilation Group. *GEBCO 2020 Grid*. 2020.
[58] NASA Ocean Biology Processing Group. *Distance to Nearest Coastline*. 2021.
[59] Copernicus Climate Change Service (C3S). *ERA5: Fifth generation of ECMWF atmospheric reanalyses of the global climate*. 2021.
[60] F. T. S. Castillo. “Floating Offshore Wind Turbines: Mooring System Optimization for LCOE Reduction”. Master’s Thesis. 2020.
[61] J. Newman and P. Owens. Properties of lightweight concrete. *Advanced concrete technology* **3** (2003), 1–29.
[62] J. Nässén et al. Concrete vs. wood in buildings–An energy system approach. *Building and environment* **51** (2012), 361–369.
[63] I. Rychlik. A new definition of the rainflow cycle counting method. *International journal of fatigue* **9**.2 (1987), 119–121.
[64] W. Mao. “Random Fatigue Analysis of Container Ship Structures”. Thesis for the degree of licentiate of engineering. Göteborg: Chalmers University of Technology, 2009.
[65] L. D. Lutes and C. E. Larsen. Improved spectral method for variable amplitude fatigue prediction. *Journal of Structural Engineering* **116**.4 (1990), 1149–1164.
[66] D. S. Steinberg. *Vibration analysis for electronic equipment (2nd edition)*. John Wiley & Sons, 1998.
[67] G. Chaudhury and W. Dover. Fatigue analysis of offshore platforms subject to sea wave loadings. *International Journal of Fatigue* **7**.1 (1985), 13–19.
[68] T. Dirlik and D. Benasciutti. Dirlik and tovo-benasciutti spectral methods in vibration fatigue: a review with a historical perspective. *Metals* **11**.9 (2021), 1333.

A

Appendix: Mass of gravity anchor

Gravity anchors made of concrete are assumed to be used as anchors for the TLP.

The net weight of the anchor is

$$W = m_{Anchor} \cdot g$$

And can be calculated with the anchor's buoyancy force B and the mooring line tension T.

$$W = B + T \tag{A.1}$$

The anchor's buoyancy force is

$$B = \rho_w g V_{Anchor} \tag{A.2}$$

where

$$V_{Anchor} = \frac{m_{Anchor}}{\rho_{Concrete}}. \tag{A.3}$$

The mooring line tension is

$$T = g \cdot \frac{m_{Displacement} - m_{Platform}}{3} \tag{A.4}$$

When substituting 1.2, 1.3 and 1.4 in 1.1 we get

$$m_{Anchor} g = \rho_w g \frac{m_{Anchor}}{\rho_{concrete}} + g \frac{m_{Displacement} - m_{Platform}}{3} \tag{A.5}$$

$$m_{anchor} = \frac{m_{Displacement} - m_{Platform}}{3\left(1 - \frac{\rho_w}{\rho_{concrete}}\right)} \tag{A.6}$$

With the densities for ocean water $1025 \frac{\text{kg}}{\text{m}^3}$ and concrete $2400 \frac{\text{kg}}{\text{m}^3}$ the minimum anchor mass is

$$m_{Anchor} = 1752,4t$$

To be safe a mass of 2000t per anchor is assumed. Which results in a volume of 833 m^3.

B

Appendix: Installation costs for WindStar TLP system

Vessel type	Operation	Value	Duration	Unit cost	OW	Total cost
Lifting Operations						
Quayside Crane	Quayside lifts	3	0.08	6000	0.75	2000
Crane barge	Rigging		0.08		0.75	6111.111
	Ballast	1.00	-	55000.00	0.6	0
	2 near-shore lifts		0.38		0.72	28645.83
	Personnel usage	30	0.38	370	0.72	5781.25
Loading, Assistance and Transportation						
Tug boats	Loading	2	0.25	17000	0.75	11333.33
	Up-ending	0	0.50	17000	0.6	0
	Assistance	2	0.38	17000	0.72	17708.33
	Transportation	2	1.20	17000	0.54	75549.51
	Mooring	2	1.50	17000	0.55	92727.27
AHTS	Transportation	1	1.20	91000	0.54	202206
	Mooring	1	1.50	91000	0.55	248181.8
Total installation cost per wind turbine						690244.5
Installation cost per wind turbine without transport						412489

Table B.1: Installation costs for the WindStar TLP System for a site located 200 km offshore

C

Appendix: Winterstein correction

The correction factor for a non-gaussian distribution according to Winterstein is

$$\gamma_{ng} = \left(\frac{\sqrt{\pi}k}{2\Gamma(1+|\nu_2|)}\right)^m \left(\frac{\Gamma(1+m|\nu_2|}{\Gamma(1+\frac{m}{2})}\right), \tag{C.1}$$

where

$$k = \frac{1}{\sqrt{(1+2h_3^{*2}+6h_4^{*2}}} \tag{C.2}$$

and

$$\nu_2 = \sqrt{\frac{4}{\pi}(1+h_4+h_4^*)-1}. \tag{C.3}$$

The variables h_4, h_4^*, h_3, h_3^* are functions of the Skewness and Kurtosis and can be calculated with

$$h_4 = \frac{Ku-3}{24}, h_4^* = \frac{\sqrt{1+1.5(Ku-3)}-1}{18}, \tag{C.4}$$

$$h_3 = \frac{Sk}{6}, h_3^* = \frac{Sk}{6(1+6h_4^*)} \tag{C.5}$$

DEPARTMENT OF SOME SUBJECT OR TECHNOLOGY
CHALMERS UNIVERSITY OF TECHNOLOGY
Gothenburg, Sweden
www.chalmers.se

CHALMERS
UNIVERSITY OF TECHNOLOGY